Causality Verification and Enforcement for Microelectronic Package Macromodels

A Dissertation

Presented in Partial Fulfillment of the Requirements for the

Degree of Doctor of Philosophy

with a

Major in Electrical Engineering

in the

College of Graduate Studies

University of Idaho

by

Hazem A. Aboutaleb

May 2014

Major Professor: Aicha Elshabini, Ph.D.

Co-Major Professor: Lyudmyla Barannyk, Ph.D.

Authorization to Submit Dissertation

This dissertation of **Hazem A. Aboutaleb**, submitted for the degree of Doctor of Philosophy with a major in Electrical Engineering and titled **"Causality Verification and Enforcement for Microelectronic Package Macromodels,"** has been reviewed in final form. Permission, as indicated by the signatures and dates given below, is now granted to submit final copies to the College of Graduate Studies for Approval.

Major Professor _____ Date _____
Aicha Elshabini, Ph.D.

Co-Major Professor _____ Date _____
Lyudmyla Barannyk, Ph.D.

Committee Members _____ Date _____
Fred Barlow, Ph.D.

_____ Date _____
Brian Johnson, Ph.D.

_____ Date _____
Suat Ay, Ph.D.

_____ Date _____
Gabriel Potirniche, Ph.D.

Department Administrator _____ Date _____
Fred Barlow, Ph.D.

Discipline's College Dean _____ Date _____
Larry Stauffer, Ph.D.

Final Approval and Acceptance by the College of Graduate Studies

_____ Date _____
Jie Chen, Ph.D.

Abstract

The design and analysis phase of passive structures of high speed microelectronic systems require suitable macromodels that capture the relevant electromagnetic properties that affect the signal and power quality. These models are constructed either from direct measurements or electromagnetic simulations using macromodeling techniques such as Vector Fitting. The raw data that are used for extraction of such models have the form of discrete port frequency responses and they may be contaminated by errors due to noise, inadequate calibration techniques in case of direct measurements or approximation and discretization errors in case of numerical simulations. Besides, these data are typically available over a finite frequency range as discrete sets with a limited number of samples. All this may affect the performance of the macromodeling algorithm. Often the underlying cause of such behavior is the lack of causality in given data.

The dissertation conducts a study of system causality, starting from an overview of macromodeling of microelectronics packages, signal and power distribution networks and simultaneous switching noise. Various system causality definitions, conditions and requirements are presented. Different available methods for causality verification in time and frequency domains are discussed.

Motivated by the limitations and drawbacks associated with conventional methods of causality verification and enforcement, in particular, that the frequency responses are available on a finite bandwidth in a discrete form, the dissertation presents two new methods that check and enforce causality in the frequency domain. The methods are based on Kramers-Krönig relations, also called dispersion relations. Both methods construct a periodic continuation of the given frequency responses, so that the resulting function is periodic on a wider domain.

The first method uses periodic polynomial continuation with the subsequent use of Fast Fourier Transform to compute discrete Hilbert Transform and characterize

causality. The second approach approximates frequency responses by a Fourier series using Singular Value Decomposition (SVD) based method. Causality is imposed directly and exactly on Fourier coefficients. The two methods are successfully tested on several analytic and simulated examples that represent interconnect macromodeling systems to show excellent performance of the proposed techniques. Artificial causality violations were imposed to demonstrate that both methods are able to detect them successfully.

Acknowledgments

Apart from the efforts of myself, the success of any project depends largely on the encouragement and guidance of many others. I take this opportunity to express my gratitude to the people who have been instrumental in the successful completion of this project.

I would like to express my special appreciation and thanks to my advisor Professor Dr. Fred Barlow, He has been a tremendous mentor for me. I would like to thank him for encouraging my research and for allowing me to grow as a research scientist. His advice on both research as well as on my career have been priceless. I also like to thank my advisor Professor Dr. Aicha Elshabini for her great support and guidance.

I take this opportunity to express my gratitude and greatest appreciation to Prof. Lyudmyla Barannyk. I can not say thank you enough for her tremendous support and help. I feel motivated and encouraged every time I attend her meeting. Without her encouragement and guidance this research would not have materialized. The guidance and support received from her was vital for the success of the research. I am grateful for her constant endless support and help.

I would also like to thank my committee members, professor Brian Johnson, professor Suat Ay, professor Gabriel Potirniche for serving as my committee members and conducting my research.

A special thanks to my family. Words can not express how grateful I am to my mother, father, mother-in law, father-in-law, brother and sisters for all of the sacrifices that you have made on my behalf. My Mom, your prayer for me was what sustained me thus far and I present my achievement as a gratitude gift to you.

At the end I would like to express appreciation to my beloved small family Nour, Mohamed and my lovely wife Yasmin who incited me to strive towards my goal and spent sleepless nights with me. She was always my support in the moments when

there was no one to answer my queries. I want to thank her for her love, kindness and support that she showed during the past three years.

Thanks God for helping me accomplish this achievement.

Table of Contents

List of Tables

List of Figures

Chapter 1

Introduction

1.1 Overview

Throughout this dissertation a discussion on *Electronic Package Macromodels System Causality* is carried out trying to cover basic information about causality definitions, requirements, and conditions. The dissertation addresses different topics related to causality spanning from causality violation, non-casual problems, and sources for causality violations. Toward estimating sources for causality violations, a brief study of different methodologies for generating electronic packaging macromodels is carried out. The main part of the dissertation tackles different approaches of causality verification in both time and frequency domain with a brief explanation of different methods utilizing both approaches. Two new methods for causality characterization in the frequency domains are introduced and presented in the dissertation.

1.2 Dissertation Objectives

The frequency responses data used to generate macromodels are usually given as a discrete set of values on a finite bandwidth. Causality conditions in the frequency domain can be written as integral equations over infinite domain. The fact that the data are available only on a finite interval creates significant errors in the boundary regions that pose difficulty in causality verification. Motivated by a goal to remove such boundary artifacts, the dissertation develops two new methods for causality verification and enforcement based on periodic continuations that could avoid the limitations and drawbacks of existing conventional procedures for causality verification and enforcement.

1.3 Dissertation Organization

The dissertation is organized into seven chapters. After the introduction, Chapter 2 presents a literature review about microelectronic packages macromodeling. Chapter 3 overviews the system causality, methods for studying causality and their difficulties, that motivates the current research. Chapters 4 and 5 present and test the two new methods for causality verification and enforcement. Finally, Chapter 6 has the conclusions of the dissertation followed by a list of references used in the research.

Chapter 2

Microelectronic Macromodeling

2.1 Introduction

The continuous development in high performance digital systems in both speed and complexity necessitates creating enhanced modeling and simulation techniques for these digital systems. These modeling techniques must be both accurate and scalable enough to capture all the parasitic effects in the system and to perform system level simulation [1]-[3].

2.2 Electrical Integrity

Electrical integrity is a set of measures of the accuracy, quality and timing of data and power signals that passes through or applied to electrical circuits. At high bit rates various effects can degrade the electrical signal to the point that causes system or device to fail. Electrical integrity engineering is the task of analyzing and mitigating these effects. It is a major aspect in the process of design and fabrication of multi-GHz bandwidth interconnect systems as it is a key factor in achieving optimum design and subsequently best performance of high-speed board/system designs. Essentially, electrical integrity covers two main tasks: Signal Integrity (SI) and Power Integrity (PI) [4]-[6].

2.2.1 Signal Integrity (SI)

Signal Integrity (SI) [7]-[30] is an engineering practice and procedures with a fundamental goal of ensuring reliable high-speed data transmission. For a long time, SI was a major concern in long distance communications. Recently, SI has become an important phase of shorter transmission paths designs. This comes from the fact

that interconnects in Signal Distribution Network (SDN) can no longer be treated as electrically transparent in the system design process due to the continuous and rapid increases in clock frequencies and decreases in rise times. As the transmission speeds become comparable with the signal edge-times, interconnects must be considered as transmission lines with distributed properties, similar to microwave circuits. SI procedures optimize the design of the transmission lines in order to minimize distortion of the signals at the receivers.

SI addresses two main concerns in the electrical design aspects: signal timing and signal quality. SI ensures all transmitted signals are received correctly and in time, signals do not interfere with one another in a way to degrade reception, signals do not damage any device and finally signals do not pollute the electromagnetic spectrum. Some of the main issues that damage both signal timing and signal quality are ringing, distortion, noise, reflection noise and power/ground noise which in some cases is called Simultaneous Switching Noise (SSN) [31]-[39] as it is due to parasitics of the power/ground delivery system during drivers' simultaneous switching output. Signal integrity engineering is the task of analyzing and mitigating all these impairments.

Signal integrity is an important activity at all levels of electronics packaging and assembly, starting from internal connections of an integrated circuit (IC), through the package, the printed circuit board (PCB), the back-plane, and inter-system connections.

2.2.2 Power integrity (PI)

Power Integrity (PI) [40]-[44] of a system is the set of measures that are carried out to verify and ensure that all the devices contained in this system have the proper supply voltage to operate at their intended performance levels. The supply voltages are provided to devices through a Power Delivery Network (PDN) which is a network of interconnects that delivers power from power supply to devices through the PCB,

the package, and the on-die routing. The rapid and continuous development of high performance digital systems in both speed and complexity intensifies channel data rate and interconnection density requirements of the PCB. As the interconnection density and number of pins per device increase, the possibility of large supply noise on the chip and in the package due to SSN increases as well. More and more chip failures are being reported industry-wide, due to I/O simultaneous switching output noise.

Simultaneous switching output noise (I/O SSO) is the noise that affects both signal and supply power due to large number of output drivers switching occurring at the same time. Obviously increasing the number of output pins in the system increases the probability of I/O SSO induced noise. The simultaneous switching of output drivers creates large current surges and voltage collapse that affect the signal quality of the output drivers and the drivers in the vicinity. In addition, the supply noise and current surge in the on-chip and the package power network can be coupled into the signal, especially when the signal lines are referenced to the supply planes.

As designs move into advanced process technologies and using high-speed I/O systems, the risk of I/O SSO induced chip failures increases. This comes from the fact that in advanced process technologies supply voltages are reduced in order to lower power and oxide thickness and I/O voltage is scaled down to ease the implementation of driver circuits. These two main characteristics of advanced process technologies increases circuit's sensitivity to voltage changes due to decreasing supply voltage and consequently, this degrades the system power integrity. Moreover, the large current changes (di/dt) on the supply nets resulting from using of high-speed I/O systems with fast signal transitions cause increased voltage drop on inductive components of both package and on-chip supply nets.

2.2.3 SI and PI Co-simulation

Conventional design systems carry out PDN design and SDN design separately in the time and frequency domains respectively without taking into consideration the mutual electronic interactions between them. This trend leads to more chip failures reported industry-wide due to I/O simultaneous switching output noise. To overcome this downside, a co-design methodology [45]-[50] is used to handle signal routing and power network design simultaneously to satisfy both the power and signal integrity constraints prior to a detailed layout. This co-design methodology employs a global I/O SSO analysis that studies both direct effect and mutual interaction of chip, package and PCB designs on power integrity.

2.3 Macromodeling

Macromodel is a black box representation that captures the electromagnetic behavior of passive devices at the input/output ports to integrate it into circuit simulators. It can be constructed for a two port or a multi-ports device. The main function of macromodeling is to replace the electromagnetic behavior of the circuit with a reduced equivalent model that preserves the characteristics of the original passive circuit at the input/output ports, captures the electromagnetic behavior accurately and runs faster than the original circuit during time domain co-simulation using computer-aided design (CAD) tools such as Simulation Program with Integrated Circuit Emphasis software (SPICE).

For systems operating at high frequencies, the distributed and parasitic behavior of interconnects structure can be extracted using several integral or differential equation-based electromagnetic (EM) solvers or directly by measurements. Then, a transformation technique is required to obtain time-domain transfer functions for such passive structures from their frequency domain response [52]-[54].

The electromagnetic solvers use Maxwell's equations to compute the frequency response of the structure. On the other hand, the frequency response of the structure can be directly measured using a vector network analyzer. Both techniques present the response of the structure as frequency dependent data that represent transfer function of the structure in the form of scattering, admittance, or impedance parameters. This representation captures the behavior of the device at the input-output ports and is called a macromodel. There are different types of macromodels ranging from scalable macromodels, passive macromodels, broadband macromodels to non-linear macromodels. But since distributed interconnect networks are inherently passive, passive macromodel becomes the suitable type for modeling signal distribution networks (SDN) and power distribution networks (PDN). A passive macromodel has to satisfy the stability, passivity and causality conditions to enable time-domain simulation. Unstable, non-passive, non-casual macromodels generate an unstable time-domain response and can behave as an amplifier or an oscillator during time-domain simulation which is a non-physical behavior.

Several macromodeling techniques [56], [57], [61], [62], [65] have been proposed for converting the frequency domain response of the PDN into a format that can be integrated with the (SDN) in a time domain co-simulation. As both measurements and simulations used to find frequency domain response of the (PDN) results in sampled data over a limited frequency range, all macromodeling techniques use that band-limited frequency response data of passive structures to compute the macromodels that can be integrated into a time domain simulation.

Various macromodeling methodologies are currently available. Generally, electrical macromodels are created by capturing the frequency dependent data that represents the port behavior of the circuit either from an electromagnetic simulator or from measurements. This is done through two main steps. The first step is to acquire the electromagnetic response of the interconnect structure; $S_{nm}(jw_k)$. Normally, the

electromagnetic response of the interconnect structure is in a band-limited, discrete frequencies port parameters form. The second step is to generate package macromodel $H(jw)$ using these port parameters. Figure 2.1 illustrates these two main steps.

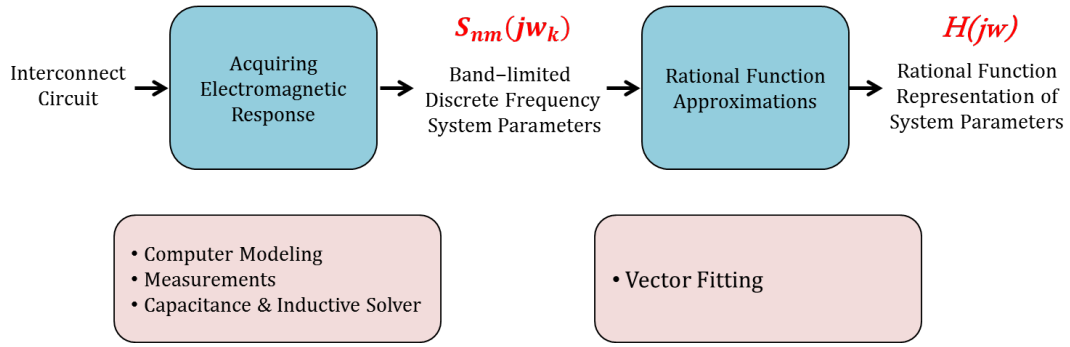

Figure 2.1: System macromodeling

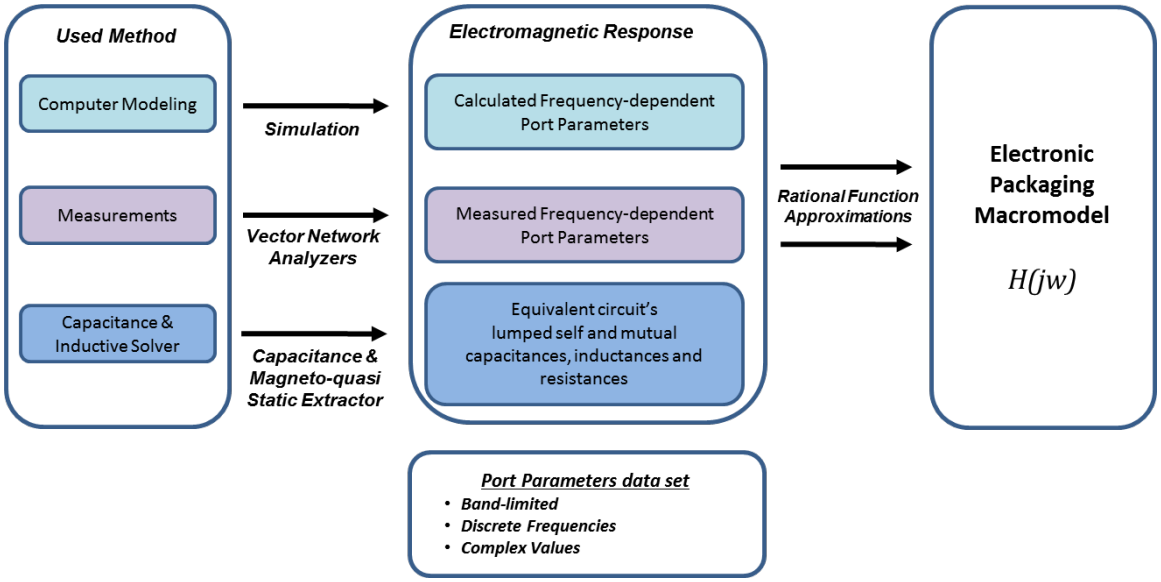

Figure 2.2: Methods of generating electromagnetic packaging macromodels

There are three main methods for acquiring electromagnetic response of a package macromodel, namely computer modeling, measurements and capacitance and inductive solver. They are shown in Figure 2.2. Computer modeling methods vary among solving parametric equations, 2D field solvers (frequency dependent RLGC tables), 2.5D field solvers or 3D full-wave electromagnetic field solvers. With this ap-

proach an electromagnetic response is acquired in the form of calculated frequency-dependent port parameters. Measurements use modern vector network analyzers (VNAs) with or without device under test (DUT) to generate measured frequency-dependent port parameters. While the capacitance and inductive solvers use capacitance extractor and magneto-quasi static extractor to find the equivalent circuit's lumped self and mutual capacitances, inductances and resistances. In all these methods, the electromagnetic response of common network representations, e.g. impedance, admittance and scattering, is obtained in a port parameter form at a discrete set of frequencies covering the finite bandwidth of interest. Well-known relationships allow the conversion from one port parameter representation to another.

To execute the second step, different macromodeling methods have been developed for building packaging macromodels using the band-limited, discrete frequency electromagnetic response data obtained from an electromagnetic simulation or measurements. These methods range from using the rational approximations of power series [56]-[58], least squares approximation [59]-[61], orthogonal polynomials [62], [63] to vector fitting [64] or by constructing of multiport broadband passive macromodels [65].

Various errors are introduced during this process. These errors may be due to noise, inadequate calibration techniques or imperfections of the test set-up in case of direct measurements or approximation errors due to the meshing techniques, discretization errors and errors due to finite precision arithmetic occurring in numerical simulations. These errors jeopardize the stability, passivity and causality of the produced macromodel or even accuracy of the obtained macromodel. To be stable, the produced macromodel need to generate bounded outputs for all bounded inputs. The passivity nature of macromodel conveys the fact that passive circuits are not capable of generating energy. If the passivity condition is not satisfied at all frequency points the passive circuit behaves as an amplifier or an oscillator during time-domain simu-

lation and generates an unstable time-domain response. On the other hand a system is called a causal system if it does not show any change in its output until its input signal is changed.

Microelectronic macromodels of passive interconnect circuits have to satisfy the system stability, passivity and causality conditions to enable proper time-domain simulations. Unstable, non-passive, or non-casual macromodels generate an unstable time-domain response and can behave as an amplifier or an oscillator during time-domain simulation which is non-physical and does not reflect correct electric properties of the system.

Chapter 3

System Causality

3.1 Overview

Throughout this chapter a discussion of causality of microelectronic package macromodel systems is carried out. It presents basic information about this topic including causality definition, causality requirements and causality conditions imposed on the system. It also addresses causality violations, sources for causality violations and problems arise from causality violation. To identify reasons for causality violations, a brief study of different methodologies for generating electronic packaging macromodels is carried out. The rest of the chapter describes various approaches and methods of causality verification and enforcement in both time and frequency domains.

3.2 Introduction

System causality is essential for extracting reliable and correct equivalent macromodels. Causal systems do not show any change in their output until their input signal changes, i.e. its output at any time t_0 is dependent only on its input for $t \leq t_0$. In other words a causal system can not anticipate changes in its input signal and its output reacts according to these changes before their occurrence, and therefore causal systems are called non-anticipatory systems. The presence of output signal proceeds input signal is called causality violation. All passive distributed interconnect networks are inherently causal and any causality violation in its equivalent macromodels results from and during the macromodel generation process itself due to numerical approximation and/or measurement errors.

3.3 Linear Time-Invariant Systems

Physical systems are modeled as linear time-invariant (LTI) systems which have two main properties. First, LTI system is a linear system i.e its response to the sum of two inputs is the sum of the responses to each input separately. Second, LTI system is a time-invariant system which implies that delaying the system input by any constant D delays the system output by the same amount.

Consider a LTI system with an impulse response function $h(t, t')$ and an input function $x(t)$ then the output response $y(t)$ can be written as a convolution of the input $x(t)$ and the impulse response $h(t - t')$ [66]:

$$y(t) = \int_{-\infty}^{\infty} h(t - t')x(t')dt' = h(t) * x(t). \tag{3.1}$$

where $(*)$ is the convolution operator.

The Fourier transform $\mathcal{F}$ of the impulse response function h, denoted by $H(w)$, is called the transfer function and it is

$$\mathcal{F}[h](w) = \int_{-\infty}^{\infty} h(\tau)\ e^{-iw\tau}d\tau \equiv H(w) \tag{3.2}$$

For multi-input/output system, the transfer function generalizes to the transfer matrix.

The primitive causality principle, stated in the time domain, says that no change in the output $y(t)$ can occur before the input $x(t)$ or, in other words, no effect can precede its cause. This implies that if $x(t) = 0$ for $t < T$, then the same is true for $y(t)$. As a consequence, the impulse response function has to satisfy the condition

$$h(t) = 0, \quad t < 0 \tag{3.3}$$

and the transfer function in Equation (3.2) becomes

$$H(w) = \int_0^\infty h(\tau)\ e^{-iw\tau} d\tau. \tag{3.4}$$

Since the integral is Equation (3.4) is extended only over a half-axis, function $H(w)$ has a regular analytic continuation in lower half w-plane.

3.4 Causality Definition

A system is causal if its output at any time t_0 is dependent only on its input for $t \leq t_0$, i.e. the system does not show any change in its output until its input signal changes, which means that its cause (output) cannot precede its effect (input). A non-causal system is manifested in the time domain as signal detected at its output before the system time delay.

3.4.1 Causality Definition in Time Domain

In time domain, a system with impulse response $h(t)$ is causal if:

$$h(t) = 0 \qquad for \qquad t < 0 \tag{3.5}$$

In practical cases, there is a propagation time associated with each circuit for the signal to travel from one input port (input) to another port (output). This time is called base delay time t_d and for general a system with impulse response $h(t)$ is causal if:

$$h(t) = 0 \qquad for \qquad t < t_d \tag{3.6}$$

Figure 3.1 shows time domain impulse response $h(t)$ of causal and non-causal systems with base delay time $t_d = 22\,\text{nsec}$. Clearly, the red and blue curves represent non causal systems as they show non-zero values before t_d. On the other hand the

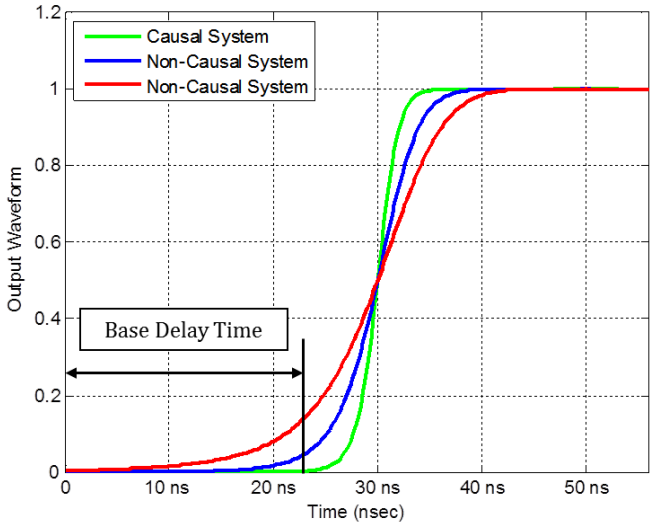

Figure 3.1: "Base time delay" causality violation

green curve represents causal systems as it shows zero output before t_d.

In this work, we assume for simplicity that the time delay is zero, i.e. $t_d = 0$.

3.4.2 Causality Definition in Frequency Domain

A system with a time domain impulse response $h(t)$ has a frequency domain transfer function $H(w)$, which is the Fourier transform of $h(t)$, and it can be written as:

$$H(w) = H_R(w) + jH_I(w) \tag{3.7}$$

where $H_R(w)$ and $H_I(w)$ are the real and imaginary parts of $H(w)$, respectively. In the frequency domain, the system is causal if $H_R(w)$ and $H_I(w)$ are related by dispersion relations [66, 67] or Kramers-Krönig conditions, namely, they satisfy

$$H_R(w) = \frac{1}{\pi} \int_{-\infty}^{\infty} \frac{H_I(w')}{w - w'} dw' \tag{3.8}$$

$$H_I(w) = -\frac{1}{\pi} \int_{-\infty}^{\infty} \frac{H_R(w')}{w - w'} dw' \tag{3.9}$$

where

$$\int\!\!\!\!\!\!-_{-\infty}^{\infty} = PV\int_{-\infty}^{\infty} = \lim_{\epsilon\to 0}\left(\int_{-\infty}^{w-\epsilon} + \int_{w+\epsilon}^{\infty}\right)$$

denotes Cauchy's principal value. The dispersion relations (3.8), (3.9) are derived under assumption that $h(t) \in L^2(\mathbb{R})$ is a square integrable function, i.e.

$$\int_0^{\infty} |h(t)|^2 dt < C$$

where C is some constant. This assumption also implies that $H(w)$ is a square integrable function [90, 95]. Kramers-Krönig conditions indicate that H_R at one frequency is related to H_I for all frequencies, and vice versa. Choosing either H_R or H_I as an arbitrary square integrable function, then the other one is completely determined by causality.

Recalling that the Hilbert Transform (HT) of $F(w)$ is defined as

$$\mathcal{H}\{F(w)\} = \frac{1}{\pi}\int\!\!\!\!\!\!-_{-\infty}^{\infty} \frac{F(w')}{w - w'} dw', \tag{3.10}$$

allows one to write equations (3.8), (3.9) as

$$H_R(w) = \mathcal{H}\{H_I(w)\} \tag{3.11}$$

$$H_I(w) = -\mathcal{H}\{H_R(w)\} \tag{3.12}$$

i.e. H_R and H_I are Hilbert transforms of each other. For this reason, dispersion relations (3.8), (3.9) are also called the Hilbert transforms integration pair. Therefore, the real and imaginary parts of a complex-valued function (transfer function) that describes electrical network properties (S-parameters, admittance, impedance, etc.) for causal systems have to be related to each other by the Hilbert transform.

3.5 Kramers-Krönig Relations

Dispersion relations were formed to reflect the causal nature of the response of materials, bodies, particles and electromagnetic fields as well. Originally, these relations were derived to prove that the light propagation is a dispersive medium [96, 97]. The classic example of a dispersion relation is the Kramers-Krönig relations that couples the real and imaginary parts of the complex transfer function of causal system.

Kramers-Krönig relations can be deduced using Fourier transform pairs. Generally, any time domain function can be represented as a sum of its even and odd parts. Thus, a system with time-domain response $h(t)$ can be represented by

$$h(t) = h_e(t) + h_o(t),$$

where $h_e(t)$ and $h_o(t)$ are even and odd components of $h(t)$, respectively. Recalling that in general $h_e(t)$ and $h_o(t)$ are complex valued functions and separating their real and imaginary parts

$$h_e(t) = h_{eR}(t) + jh_{eI}(t), \qquad h_o(t) = h_{oR}(t) + jh_{oI}(t)$$

we can write

$$h(t) = h_{eR}(t) + jh_{eI}(t) + h_{oR}(t) + jh_{oI}(t). \tag{3.13}$$

In the frequency domain, the corresponding transfer function $H(w)$ is

$$H(w) = H_{eR}(w) + jH_{eI}(w) + H_{oR}(w) + jH_{oI}(w) \tag{3.14}$$

where

$$H_e(w) = H_{eR}(w) + jH_{eI}(w), \qquad H_o(w) = H_{oR}(w) + jH_{oI}(w)$$

are even and odd components of the transfer function $H(w)$ in the frequency domain, respectively.

Recalling that:

- the Fourier transform of a real even function is a real even function.
- the Fourier transform of a purely imaginary even function is a purely imaginary even function.
- the Fourier transform of a real odd function is a purely imaginary odd function.
- the Fourier transform of purely imaginary odd function is a real odd function.

Thus the different components of $H(w)$ can be related to their correspondings in time domain of $h(t)$ through the following Fourier Transform $\mathcal{F}$ relationships:

$$\begin{aligned} H_{eR}(w) &= \mathcal{F}\{h_{eR}(t)\} \\ H_{eI}(w) &= \mathcal{F}\{h_{eI}(t)\} \\ H_{oR}(w) &= \mathcal{F}\{h_{oI}(t)\} \\ H_{oI}(w) &= \mathcal{F}\{h_{oR}(t)\} \end{aligned} \tag{3.15}$$

Since a causal system is a real system, its impulse response function $h(t)$ is real. Hence,

$$h_{eI}(t) = 0, \qquad h_{oI}(t) = 0,$$

which implies

$$H_{eI}(w) = 0, \qquad H_{oR}(w) = 0.$$

Therefore, for real systems

$$H(w) = H_{eR}(w) + jH_{oI}(w)$$

and

$$h(t) = h_{eR}(t) + h_{oR}(t),$$

where $h_{eR}(t)$ and $h_{oR}(t)$ can be written as

$$h_{eR}(t) = \frac{1}{2}[h(t) + h(-t)], \qquad h_{oR}(t) = \frac{1}{2}[h(t) - h(-t)]$$

For a causal system $h(t) = 0$, $t < 0$, and to satisfy this condition:

$$h_{oR}(t) = \begin{cases} -h_{eR}(t) & t < 0, \\ h_{eR}(t) & t > 0. \end{cases}$$

Using $\mathrm{sgn}(t)$ function

$$\mathrm{sgn}(t) = \begin{cases} -1 & \text{if } t < 0, \\ 0 & \text{if } t = 0, \\ 1 & \text{if } t > 0. \end{cases}$$

one can write

$$h_{oR}(t) = \mathrm{sgn}(t) h_{eR}(t).$$

Thus,

$$h(t) = h_{eR}(t) + \mathrm{sgn}(t) h_{eR}(t)$$

In frequency domain this is equivalent to

$$H(w) = \mathcal{F}\{h_{eR}(t) + \mathrm{sgn}(t) h_{eR}(t)\}$$

$$H(w) = \mathcal{F}\{h_{eR}(t)\} + \mathcal{F}\{\mathrm{sgn}(t) h_{eR}(t)\} \tag{3.16}$$

$$H(w) = \mathcal{F}\{h_{eR}(t)\} + \mathcal{F}\{\mathrm{sgn}(t)\} * \mathcal{F}\{h_{eR}(t)\} \tag{3.17}$$

$$H(w) = H_{eR}(w) + \frac{1}{j\pi w} H_{eR}(w), \tag{3.18}$$

Writing the Hilbert transform $\mathcal{H}\{H_e(w)\}$ of $H_e(w)$ as

$$\mathcal{H}\{H_e(w)\} = \frac{1}{\pi w} * H_e(w), \tag{3.19}$$

that is equivalent to

$$\mathcal{H}\{H_e(w)\} = -\frac{1}{\pi}\int_{-\infty}^{\infty} \frac{H_e(w')}{w - w'} dw' \tag{3.20}$$

Thus, equation (3.18) can be rewritten as

$$H(w) = H_e(w) - j\mathcal{H}\{H_e(w)\} \tag{3.21}$$

Comparing equation (3.21) with equation (3.7) implies that

$$H_R(w) = H_e(w) \qquad H_I(w) = -\mathcal{H}\{H_e(w)\} \tag{3.22}$$

which implies that the imaginary part of causal system transfer function is related to the real part through the Hilbert transform function

$$H_I(w) = -\mathcal{H}\{H_R(w)\} \tag{3.23}$$

Similarly, we can verify that

$$H_R(w) = \mathcal{H}\{H_I(w)\} \tag{3.24}$$

Equations (3.23) and (3.24) are equivalent to

$$H_I(w) = -\mathcal{H}\{H_R(w)\} = -\frac{1}{\pi}\int_{-\infty}^{\infty} \frac{H_R(w')}{w - w'} dw \tag{3.25}$$

and

$$H_R(w) = \mathcal{H}\{H_I(w)\} = \frac{1}{\pi}\int_{-\infty}^{\infty} \frac{H_I(w')}{w - w'} dw, \tag{3.26}$$

which are the same equations as (3.9), (3.8), respectively.

3.6 Causality Violation Problems

It is important to study the harmful effects of dealing with system causality violations, and in order to explain these effects some facts must be clarified. In the frequency domain, the lack of causality in discrete port frequency responses may affect the process of generating the system macromodel resulting in non-convergence or inaccurate models [92]. Using such macromodels in a time-domain analysis may cause serious problems, such as non-physical transient responses and/or simulation failures. Moreover, causality has a great effect on system stability in the discrete domain where the practical workplace sampled data gets analyzed [68], noncasual system may produce a non-stable system in the discrete domain which complicates and prevents time domain analysis of the system. In addition, causality problems lead to large errors in predicting performance of interconnects which increases the Bit Error Rate (BER) of the system. Obviously, this occurs as the system shows output that precede the correct sampling points.

Possible sources and reasons for causality violations depend on the method that was used to create a macromodel that represents interconnects, how this macromodel was developed and what kind of data was used to produce it. In order to determine possible sources resulting in causality violations and consequently eliminate and prevent their effects, a good study of a system macromodeling process should be carried out.

3.7 Possible Sources of Causality Violation

Sources of causality violations vary depending on the method used for macro-modeling. The approach that utilizes computer modeling and capacitance and inductive solvers for acquiring electromagnetic response suffers from introduced simulation approximation errors. These errors are due to using meshing techniques, intrinsic discretization of equations, finite precision of the computing implementation, and post-processing of the data. In addition, neglecting the frequency dependence of material properties is one of the major sources of simulation approximation errors that cause a violation of the Kramers-Krönig relationship that describes the relationship between the real and imaginary parts of the permittivity of the model. At least one or both real and imaginary components of the material properties must be frequency dependent in order to satisfy the Kramers-Krönig relationship.

In case of using vector network analyzers for acquiring electromagnetic response through measurements, errors span from measurement accuracy, calibration techniques and accuracy to the possible imperfection of the test set-up. On the other hand, post-processing of the obtained data using interpolation and curve fitting of PDN frequency domain response may lead to inaccurate and probably non-causal systems.

3.8 Causality Verification and Enforcement Techniques

Generally, there are two main approaches to verify and enforce system causality: the time domain approach and the frequency domain approach [68] as it appears in Figure 3.2.

The time domain approach utilizes the primitive time domain definition of causality through studying the signal flow graph of an impulse response that represents the system performance (Eye diagram) to make sure that there is no nonzero

value of the output signal found before starting time. For more details, please see the next section. The frequency domain approach is based on the frequency domain definition of causality through dispersion relations, i.e. verifying that the real and imaginary parts of a causal function are related by Hilbert Transform integration pair. Hilbert transform can be implemented via both direct numerical integration and indirect interpolations using various kernels like Hermitan, sinc and rational functions as well as Fourier series that we use in Section 5 where we discuss our causality enforcement method based on spectral continuation. Another method that belongs to the frequency domain approach is the minimum phase and all-pass decomposition method.

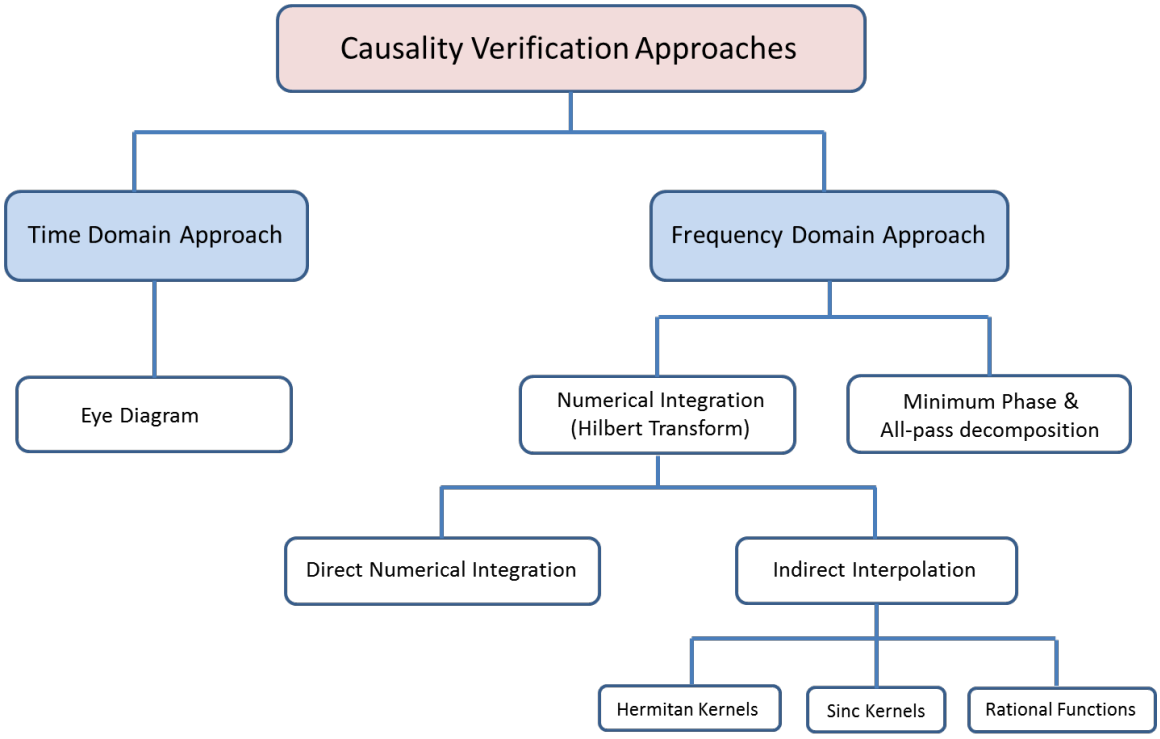

Figure 3.2: Main approaches for causality verification.

3.9 Time Domain Approach

The time domain approach utilizes the time domain definition of causality through studying the output waveform in time domain. A system is called *non-causal* in a nonzero value of $h(t)$ is found before the base delay time t_d [69]. The base delay of a component is the propagation time that passes before an input signal with certain frequency reaches the output port. Therefore, it is more accurate to check for "base delay" causality rather than checking for absolute time zero causality.

This approach is carried out through three main steps, and it is illustrated in Figure 3.3.

1. Reconstruct output waveform from its Fourier coefficients.
2. Estimate component base time delay for each input/output port pair and different operating frequency.
3. Perform causality verification by studying the waveform eye diagram to determine if there is no output before the base time delay.

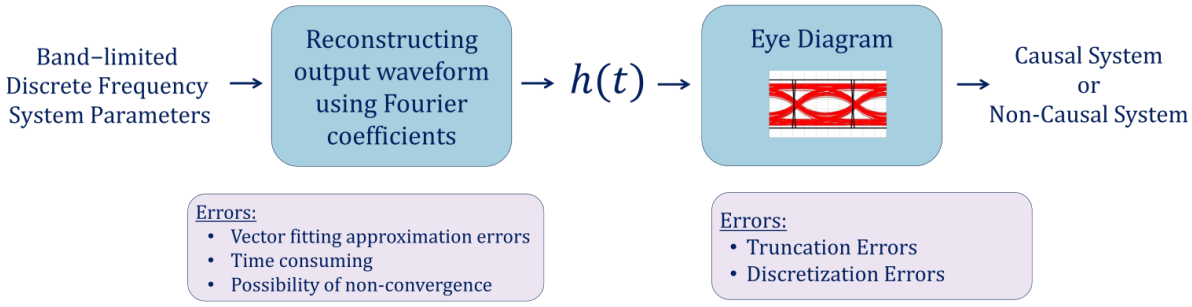

Figure 3.3: Time domain causality verification.

3.9.1 Eye Diagram

Eye diagram is a visual tool for wide system performance measures and a common indicator of the quality of signals in high-speed digital transmissions. Essentially, eye

diagram is an oscilloscope display in which a digital data signal from a receiver is repetitively sampled and applied to the vertical input, while the data rate is used to trigger the horizontal sweep. This process results in a synchronized superposition of all received bits of the signal of interest viewed within a particular signaling interval. Ideal eye diagrams appears as rectangular boxes. In reality, communications are imperfect, so the bit transitions do not line perfectly on top of each other, and an eye-shaped pattern results.

Eye diagram is used as an experimental tool for the evaluation of the combined effects of channel noise and inter-symbol interference on the performance of a base-band pulse-transmission system. In addition it can be used in system causality verification by visually inspecting the produced diagram and assure that no output signal precedes the base time delay.

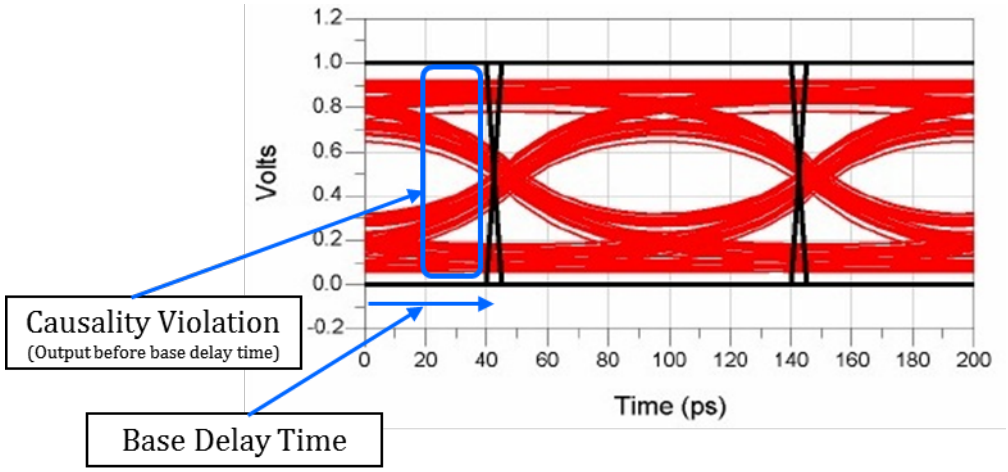

Figure 3.4: Non-causal system eye diagram.

Figures 3.4 and 3.5 show how the eye diagram is used in causality check where a signal flow graph of several PRBS (pseudorandom binary sequence) patterns running at 10 Gbps are displayed. The black waveforms in figures represent the component's "base delay".

In Figure 3.4 the red waveform represents non-causal system as it shows output before base time delay in black. The causality violation appears in the blue box and

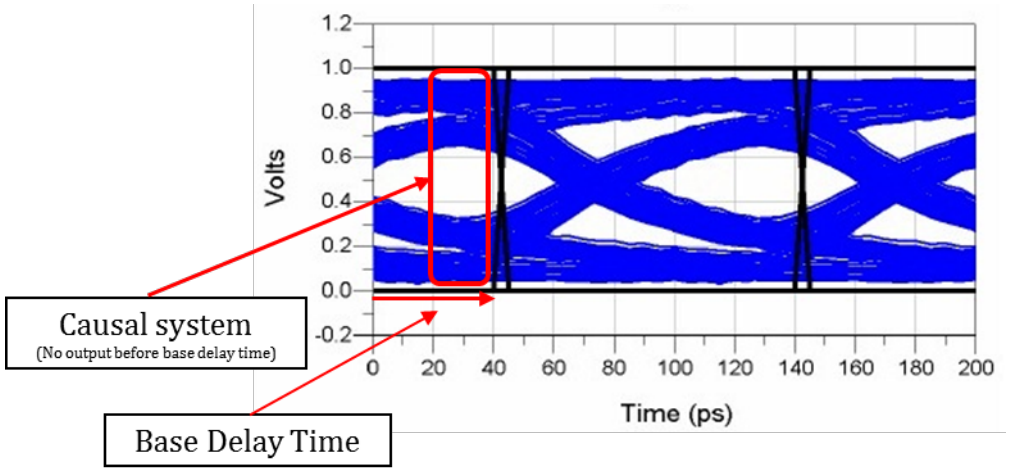

Figure 3.5: Causal system eye diagram.

the eye pattern does not display the expected "shark fin" wave shape. Whereas, the blue waveform in Figure 3.5 represents a causal system due to the absence of output before base time delay as it clearly appears in the red box.

Unfortunately, this approach suffers from Gibbs phenomenon due to using truncated Fourier series for discontinuous functions as we demonstrate in the next Section.

3.9.2 Gibbs Phenomenon

Gibbs phenomenon illustrated in Figure 3.6 is inherent in Fourier analysis for functions that are not smooth enough and have discontinuities, which is typical for transfer functions of interconnects.

The transfer function of an interconnect is usually highly discontinuous due to delayed reflections and it is often composed of series of spikes. In addition, its values are available only on a finite sample frequency interval. Reconstructing, for example, a square pulse signal with a finite number of jump discontinuities, which is a piecewise constant function, in the time domain using a truncated Fourier series leads to a signal waveform that very close to the original signal except with rippling around the discontinuities. The more Fourier coefficients are used, the more the constructed signal begins to resemble the original signal. At the same time, the ripples get narrow,

but do not disappear (see the right panel of Figure 3.6). For a discontinuous function even when the large number of Fourier coefficients used, the main undershoot and overshoot will alway exist and their height will remain about 9% of the pulse height jump.

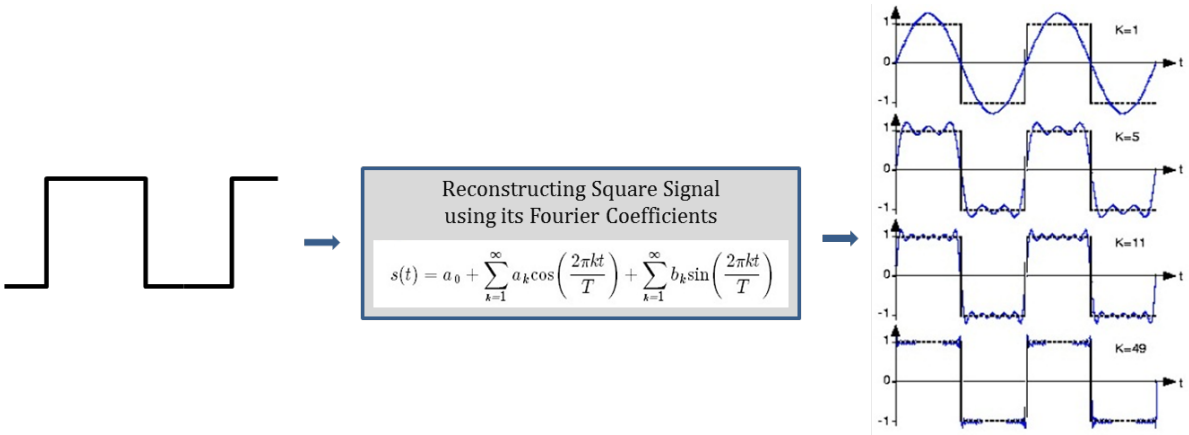

Figure 3.6: Square signal Fourier series approximation.

The pre-cursor ripples in an impulse response function are the combination of Gibbs oscillations and possible non-casual signals. Thus time domain approach for causality check is practically difficult to be implemented because it is hard to separate a true causality violation from Gibbs errors. Windowing is the classical technique to reduce Gibbs error but unfortunately it only compresses Gibbs oscillations rather than completely eliminates them [75]. Another limitation of this approach is that it is a method of causality verification only and it is not capable of causality enforcement.

3.10 Frequency Domain Approach

Frequency domain approach utilizes the fact that the real and imaginary parts of a casual transfer function $H(w)$ are related through Hilbert transforms or satisfy Kramers-Krönig relations (3.8), (3.9). For more details, please see Section 3.4.2. Therefore, causality verification is done by checking whether the real and imaginary parts of the frequency response of interconnects satisfy Kramers-Krönig relations

(3.8), (3.9).

Verifying causality using frequency domain approach is a preferred method since the data representing interconnects are usually given in the frequency domain [70]. Generally this data is a set of frequency response values that have been measured or simulated over a set of discrete frequency points that covers a band-limited frequency range.

Frequency domain approach for causality verification is normally carried out through calculation of the Hilbert Transform of, say, the real part of H and then comparing the result with the imaginary part of H, or vice versa, using equations (3.8), (3.9). Since the Hilbert Transform is an integral operator, the implementation of this approach can be done by applying numerical integration methods [64, 71] via either direct numerical integration [71, 72], indirect interpolations using various kernels like Hermitan [73], sinc [74], or using rational functions [64]. In our causality characterization method based on spectral continuation that is presented in Section 5, we do not compute Hilbert Transform numerically. Instead, we impose causality condition directly and exactly on Fourier coefficients used to approximate the transfer function.

3.10.1 Direct Numerical Integration Method

In this method the Hilbert Transform is used as a tool to assess the consistency of measured or numerically computed network transfer functions with respect to the causality conditions [71]. The Hilbert transform is a commonly used technique for relating the real and imaginary parts of a causal spectral response. It is found in both continuous and discrete forms. A direct numerical integration of Hilbert Transform is applied by computing the integration in Equations (3.25) and (3.26) using the linearity properties of these relations that enables simplifying the complicated integrations by breaking them down into pieces and compute them individually [71, 72].

3.10.2 Indirect Interpolations Methods

Hilbert transform can be implemented via indirect interpolation using various kernels like Hermitan, sinc and rational functions as it is explained in the next subsections.

Hermitan Series Expansion Method

The time-domain response of a passive structure is modeled as an associate Hermite series expansion [73]. Using the isomorphism of the associate Hermite function and its Fourier transform, the frequency-domain response can be expressed as a scaled version of the time-domain expansion. Using early-time and low-frequency data, this method demonstrates simultaneous expansion in both domains. Expansions with only 10 - 20 terms give good enough extrapolation in both time and frequency domains. The computation involved in this method is minimal.

Sinc Series Expansion Method

This algorithm permits the reconstruction of a band-limited function from samples taken at not necessarily regularly spaced intervals, and also the recovery of the Hilbert transform of the function [74]. It enables the reconstruction of the real or the imaginary parts of the dielectric permeability by means of the Kramers-Krönig relations. Regardless of the given sampling values, the algorithm converges in L^2 as well as point-wise. In contrast to popular methods that implement Kramers-Krönig relations, this algorithm requires no computation of Fourier integrals. Only a system of linear equations has to be solved in each iteration step. The approximating functions are distinguished by minimal energy.

Rational Functions Approximation Method

This method is the most widely used tool for causality verification. It uses a general methodology - known as vector fitting - for approximating measured or calculated frequency domain responses by a rational function. The vector fitting is an iterative procedure in which an initial set of poles is replaced with an improved set of poles via a scaling procedure [64], and the corresponding residues are computed. Frequency domain approach for causality verification using rational function approximations is normally carried out through two main steps, which are illustrated in Figure 3.7.

1. Fit the measured or simulated band-limited discrete frequency system parameters $S_{nm}(jw_k)$ to a rational function representation $H(w)$ [64]:

$$H(w) = a_m \frac{(jw - Z_1)(jw - Z_2)(jw - Z_3)\cdots(jw - Z_m)}{(jw - P_1)(jw - P_2)(jw - P_3)\cdots(jw - P_n)} \tag{3.27}$$

   where $Z_1, Z_2, \ldots, Z_m$ are zeros and $P_1, P_2, \ldots, P_n$ are poles of the transfer function $H(w)$, respectively.

2. Calculate the Hilbert Tranform integration pair using dispersion equations (3.8), (3.9) with the rational function representation (3.27) produced in Step 1 by applying numerical integration methods [64, 71].

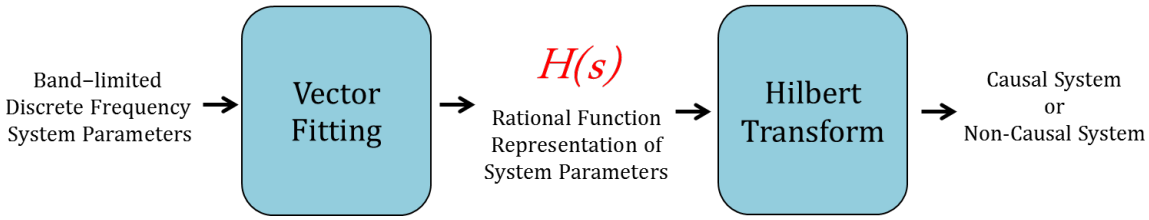

Figure 3.7: Conventional frequency domain causality verification and enforcement method.

3.10.3 Minimum Phase and All-Pass Decomposition Method

This method is based on the minimum-phase and all-pass decomposition technique from classical digital signal processing practices [68]. Compared with other methods based on Hilbert transform, this method demonstrates fewer requirements to the frequency band. Fast implementation of Hilbert transform based on FFT/IFFT is used but Gibbs errors are not found problematic.

Implementation of this method starts with decomposing the z-transform $H(z)$ of a real, causal and stable impulse response $h(t)$ into the product of a minimum-phase term and an all-pass terms:

$$H(z) = H_{min}(z)H_{ap}(z) \tag{3.28}$$

where $H_{min}(z)$ is the minimum-phase term with its zeroes and poles within the unit circle, and $H_{ap}(z)$ is the all-pass term that has its poles and zeros forming conjugate reciprocal mirrors across the unit circle.

Recalling the fact that a noncasual sequence and its causal counterpart have an identical z-transform with different regions of convergence (ROC) as the only difference to set them apart. A noncasual sequence has its ROC extending inward from the innermost pole while a causal sequence has its ROC extending outward from the outermost pole. Then, the causality check problem is translated into a problem of searching for unstable poles in the frequency response of interconnect. This can be done by examining the phase plot of the corresponding all-pass function.

3.11 Frequency Domain Approach Difficulties

The frequency domain approach for causality characterization also has a number of drawbacks and potential errors [70]. Causality in the frequency domain is defined through dispersion relations (3.8), (3.9) that are integral equations with integration

extended over an infinite domain (or semi-infinite if spectral symmetry of transfer functions as Fourier transforms on real-valued impulse response function is used). However, the port responses are typically available as a discrete set of system parameter values obtained from measurements or simulations over a set of *discrete frequency points* that covers a *band-limited frequency range* from $w_{min} \geq 0$ to w_{max}.

3.12 Research Target

Motivated by the desire of avoiding the limitations and drawbacks associated with the conventional existing procedures for causality verification and enforcement (Gibbs phenomenon, approximation errors, truncation errors, discretization errors, finite band frequency interval and time consumption) this research investigates the possibility of deducing new methods for causality verification and enforcement in the frequency domain that will deals with the problem of having frequency responses over a finite frequency interval that causes significant boundary artifacts when the dispersion relations (3.8), (3.9) are used to verify and enforce causality.

Chapter 4

Causality Verification and Enforcement Using Periodic Polynomial Continuations

4.1 Introduction

As was mentioned in Chapter 3, causality condition in the frequency domain can be expressed via dispersion relations or Kramers-Krönig conditions (3.8), (3.9). If the impulse response function $h(t)$ (time-domain function) is real-valued, then $H_R(w)$ and $H_I(w)$ are even and odd functions, respectively. Using these symmetries in (3.8), (3.9) produces

$$H_R(w) = \frac{2}{\pi}\int_0^\infty \frac{w' H_I(w')}{(w')^2 - w^2} dw', \tag{4.1}$$

$$H_I(w) = -\frac{2w}{\pi}\int_0^\infty \frac{H_R(w')}{(w')^2 - w^2} dw'. \tag{4.2}$$

Practical application of dispersion relations (3.8), (3.9) or (4.1), (4.2) poses some difficulties. The transfer function $H(w)$ is usually available only at a discrete set of frequencies over a finite bandwidth $[w_{min}, w_{max}]$, with $w_{min} \geq 0$, while the range of integration in (4.1), (4.2), for example, extends from zero to infinity. Dispersion relations require numerical evaluation of the singular integrals but the bandwidth may not be sufficiently wide for convergence. Dispersion relations (3.8), (3.9) were derived under an assumption that the transfer function $H(w)$ is square integrable. However, in some cases $H(w)$ may not be square integrable at all and may only be bounded or behave as $O(w^n)$, when $|w| \to \infty$, $n = 0, 1, 2, \ldots$. Direct application of dispersion relations (4.1), (4.2) may result in a significant truncation error in boundary regions of the given frequency interval $[w_{min}, w_{max}]$ producing significant boundary artifacts. The generalized dispersion relations or dispersion relations with subtractions [98,

66] can be used to increase the convergence of the dispersion integrals by making integrands less sensitive to the high-frequency behavior of $H(w)$, and, thus, reduce the reconstruction errors caused by the finite bandwidth. This approach has been successfully used in [67, 70, 99] to develop a causality verification tool for bandlimited tabulated frequency responses. A recent paper [100] employes the dispersion relations with subtractions to improve accuracy of vector network analyzer (VNA) scattering parameter device characterization. However, even using the dispersion relations with subtractions does not completely remove the boundary artifacts.

In general, for a decaying impulse response function $h(t)$, the asymptotic behavior of its Fourier transform $H(w)$ may approach a constant H_∞ as $|w| \to \infty$. This would imply that the impulse response function $h(t)$ has a delta function present at $t = 0$. For impulse response functions that do not contain such singularities, $H_\infty = 0$. Writing $H_\infty = R_\infty + iI_\infty$, the dispersion relations become [101]

$$H_R(w) = \frac{1}{\pi}\int_{-\infty}^{\infty} \frac{H_I(w')}{w - w'}dw' + R_\infty, \tag{4.3}$$

$$H_I(w) = -\frac{1}{\pi}\int_{-\infty}^{\infty} \frac{H_R(w')}{w - w'}dw' + I_\infty. \tag{4.4}$$

Because of the odd symmetry of H_I and its uniqueness, $I_\infty = 0$. Hence, (4.3), (4.4) become

$$H_R(w) = \frac{1}{\pi}\int_{-\infty}^{\infty} \frac{H_I(w')}{w - w'}dw' + R_\infty, \tag{4.5}$$

$$H_I(w) = -\frac{1}{\pi}\int_{-\infty}^{\infty} \frac{H_R(w')}{w - w'}dw'. \tag{4.6}$$

Generalized dispersion relations (4.5), (4.6) imply that H_I can be determined from H_R, while H_R is determined from H_I to within a constant. This suggests that when it is not known that $H(w)$ should decay to zero as $|w| \to \infty$, causality can be verified by reconstructing H_I from H_R and comparing the result with the given H_I, while reconstructing H_R from H_I would require the knowledge of R_∞. For this

reason, in what follows we will use H_R to reconstruct H_I. Equations (4.5), (4.6) can be used to reconstruct H_R to reconstruct H_I or their analogues of (4.1), (4.2) with constant R_∞ added to the right hand side of (4.1). Therefore, to verify causality, one would need to truncate the domain of integration and integrate singular integrals numerically.

An alternative formulation can be obtained using convolution operation. Indeed, we can write (4.5), (4.6) as

$$H_R(w) = \frac{1}{\pi w} * H_I(w) + R_\infty, \tag{4.7}$$

$$H_I(w) = -\frac{1}{\pi w} * H_R(w). \tag{4.8}$$

Convolution can be computed using Fourier transform $\mathcal{F}$ and its inverse $\mathcal{F}^{-1}$ via convolution theorem to give

$$H_R(w) = \mathcal{F}^{-1}\left[\mathcal{F}\left[\frac{1}{\pi w}\right] \cdot \mathcal{F}[H_I(w)]\right] + R_\infty, \tag{4.9}$$

$$H_I(w) = -\mathcal{F}^{-1}\left[\mathcal{F}\left[\frac{1}{\pi w}\right] \cdot \mathcal{F}[H_R(w)]\right]. \tag{4.10}$$

Equations (4.9), (4.10) provide another way of reconstructing H_I from H_R and vice versa. Discrete Fourier transform and its inverse can be computed employing FFT/IFFT subroutines. However, these techniques are designed for periodic functions while the transfer functions $H(w)$ are not periodic in general. Direct application of FFT/IFFT to non-periodic data may result in significant boundary errors. To overcome this difficulty, we construct a smooth polynomial periodic continuation $\mathcal{C}(H_R)$ of $H_R(w)$ on a wider domain. Then this periodically continued function can be used to reconstruct H_I employing FFT and IFFT routines. H_I can be also be used to reconstruct H_R, however, as can be seen from equation (4.9), this would require the

knowledge of R_∞. For this reason, it makes sense to reconstruct H_I from H_R unless it is known that $R_\infty = 0$. The idea of using periodic continuation was motivated by an example of the function $H(w) = e^{-iaw}$, $a > 0$, that is not square integrable and only bounded but satisfies the dispersion relations and has periodic real and imaginary parts. Indeed, $H_R = \cos(aw)$, $H_I = -\sin(aw)$ and $\mathcal{H}(\cos(aw)) = \sin(aw)$ and $\mathcal{H}(\sin(aw)) = -\cos(aw)$.

In this work, we propose a method for causality characterization based on the dispersion relations and smooth periodic polynomial continuation of the transfer function. The approach significantly (by a several of orders of magnitude) decreases reconstruction errors caused by the finite bandwidth compared to the direct application of the dispersion relations without any continuation. The method is also capable of detecting small localized causality violations. The details are presented next.

4.2 Periodic Polynomial Continuation

In applications, the transfer function $H(w)$ is available on a finite bandwidth $[w_{min}, w_{max}]$, $w_{min} \geq 0$, with a limited number of discrete values. We start with the baseband case when $w_{min} = 0$. The approach can be generalized to the bandpass case when $w_{min} > 0$ as we show later. Using spectrum symmetry, we can define $H(w)$ for $[-w_{max}, 0]$, since H_R and H_I are even and odd functions, respectively. For convenience, we rescale $H(w)$ to $H(x)$ defined on $x \in [-0.5, 0.5]$ by substitution $x = \frac{0.5}{w_{max}} w$. Starting from H_R, we construct a new function $\mathcal{C}(H_R)$, the periodic continuation of H_R, that is the same as H_R on the interval $[-0.5, 0.5]$ and defined by an mth degree polynomial $P_m(x)$ on $[0.5, 0.5 + 2b]$ in such a way that this new function is periodic in the extended domain of length $1+2b$. In addition, this function and its derivatives up to order $m/2+1$ inclusively are continuous at $x = \pm 0.5$. Given a function $H_R(x)$, available at a discrete set of points in a unit-length interval, its

periodic mth degree polynomial continuation $\mathcal{C}(H_R)$ is defined by

$$\mathcal{C}(H_R) = \begin{cases} H_R(x), & x \in [0, 0.5] \\ H_R(-x), & x \in [-0.5, 0] \\ P_m(x) = \sum_{l=0}^{m} \alpha_l (x - x_0)^l, & x \in [0.5, 0.5 + 2b], \quad x_0 = 0.5 + b \end{cases} \tag{4.11}$$

where function $H(x)$ was reflected to $[-0.5, 0]$ as an even function and $1 + 2b$ is the period of the continuation. Since H_R is the even function, the polynomial P_m should be of even degree m and the polynomial $\sum_{l=0}^{m} \alpha_l x^l$ should be an even function as well. Hence, all coefficients α_l with odd indices are zero. The remaining coefficients α_l with even indices are computed by requiring $P_m(x)$ and its derivatives to match function H_R and its corresponding derivatives at points ± 0.5. By symmetry, it is enough to consider only the point $x = 0.5$. For example, for $P_2(x) = a_2(x - x_0)^2 + a_0$ the unknown coefficients are a_2 and a_0 and they are computed by requiring P_2 and $\frac{d}{dx}(P_2)$, to match H_R and $\frac{d}{dx}(H_R)$, respectively, at $x = 0.5$. For $P_4(x) = a_4(x - x_0)^4 + a_2(x - x_0)^2 + a_0$, the unknowns a_4, a_2 and a_0 are computed by requiring P_4, $\frac{d}{dx}(P_4)$, $\frac{d^2}{dx^2}(P_4)$ to match H_R, $\frac{d}{dx}(H_R)$, and $\frac{d^2}{dx^2}(H_R)$ at $x = 0.5$, respectively. A polynomial P_{2k} has $k + 1$ unknown coefficients that are found by requiring P_{2k} and its derivatives up to order k inclusively to have the same values as H_R and its corresponding derivatives at $x = 0.5$.

To compute coefficients α_l of the polynomial $P_m(x)$, one needs to know function H_R and its derivative(s). However, only discrete values of H_R are available. Derivatives of H_R can be approximated, for example, using one-sided finite differences [102], since only values of $H(x)$ to the left from point $x = 0.5$ are available. Higher order approximations of derivatives can be constructed using, for instance, Richardson extrapolation [102].

In Figure 4.1, as an example, we show function $4x^4 + 4x^2 + 1$ and its periodic 8th degree polynomial continuation with $b = 0.1$. The resulting continuation and its

derivatives up to 4th order are continuous at $x = \pm 0.5$.

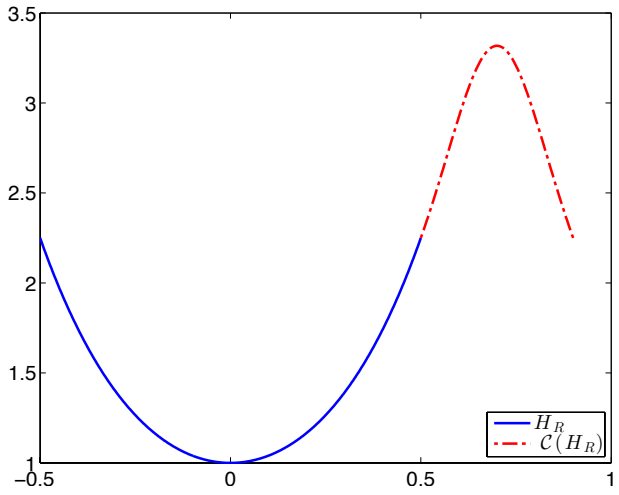

Figure 4.1: Function $4x^4+4x^2+1$ and its periodic 8th degree polynomial continuation with $b = 0.1$.

Once $\mathcal{C}(H_R)$ is constructed, it can be employed to compute $\mathcal{C}(H_I)$ on $[-0.5, 0.5+2b]$ using equation (4.10) and FFT/IFFT to compute direct and inverse discrete Fourier transforms. The result is then compared with H_I on the original interval $[-0.5, 0.5]$. Denote by E_C the absolute error in reconstructing H_I from H_R using a polynomial continuation:

$$E_C = H_I - \mathcal{H}[\mathcal{C}(H_R(x))], \quad x \in [-0.5, 0.5]. \tag{4.12}$$

For completeness, we also introduce the absolute error E of reconstructing H_I from H_R without any continuation used:

$$E = H_I - \mathcal{H}[H_R(x)], \quad x \in [-0.5, 0.5]. \tag{4.13}$$

Given a tolerance $\epsilon > 0$, and computing some norm $||E_C||$ (l_∞ or l_2 norm, for example) of the reconstruction error E_C, a decision can be then made whether the given transfer function $H(x)$ is causal or not depending if $||E_C|| < \epsilon$ or not.

The above approach can also be generalized to the bandpass regime with $w_{min} > 0$. In this case, $H(w)$ is available at a discrete set of points in $[w_{min}, w_{mx}]$. Similarly to the baseband case, we rescale $H(w)$ to $H(x)$ by substitution $x = \frac{0.5}{w_{max}} w$. Then $H(x)$ is defined on $[a, 0.5]$, where $a = 0.5\frac{w_{min}}{w_{max}} > 0$. Since H_R is an even function, we have values of H_R on $[-0.5, -a]$ by spectrum symmetry. To define missing values of H_R in $[-a, a]$, we construct an even degree polynomial $\tilde{P}_{m_0}$ using a similar approach as for construction of P_m, in which we require $\tilde{P}_{m_0}$ and its derivatives to match H_R and its corresponding derivatives at $x = \pm a$. The degree m_0 may be same as m or different. Then the periodic continuation $\mathcal{C}(H_R)$ is defined as follows.

$$\mathcal{C}(H_R) = \begin{cases} H_R(x), \quad x \in [a, 0.5], \\ H_R(-x), \quad x \in [-0.5, -a], \\ P_m(x) = \sum_{l=0}^{m} \alpha_l (x - x_0)^l, \quad x \in [0.5, 0.5 + 2b], \quad x_0 = 0.5 + b, \\ \tilde{P}_{m_0}(x) = \sum_{k=0}^{m_0} \beta_k x^k, \quad x \in [-a, a]. \end{cases} \tag{4.14}$$

The bandpass case is considered in a transmission line example 4.3.2, where the transfer function $H(w)$ is only available for $w > 0$.

In the next section, we test the polynomial continuation method for causality verification on several analytic and simulated causal and non-causal examples. Causal transfer functions are used for validation of the method and they present so called ideal causality test. We also impose localized causality violations and show that the approach is capable of detecting them even when the amplitude of such violations is small.

4.3 Numerical Examples

In this section, we apply the causality characterization technique based on periodic polynomial continuation described in the previous section to several analytic and simulated examples that are causal or non-causal. The causal transfer functions provide ideal causality test cases that would validate the method. For non-causal transfer functions, the approach should be able to detect the causality violation locations and indicate how far the function is from being causal.

4.3.1 Study Case I: Two-pole Transfer Function

We consider a transfer function with two poles defined by

$$H(w) = \frac{r}{iw + p} + \frac{\bar{r}}{iw + \bar{p}}. \tag{4.15}$$

with $r = 1 + 3i$ and $p = 1 + 2i$. This function was used in [91] to study extraction of time delay that is set to zero in the current work. Since the poles of $H(w)$ are located in the upper half w-plane at $\pm 2 + i$, this function is causal as it is a sum of two causal transforms. $H(w)$ was sampled on $[0, w_{max}]$ with $w_{max} = 10$ GHz. The frequency interval is scaled to $[0, 0.5]$ by the substitution $x = 0.5/w_{max}$ to obtain a rescaled function $H(x)$. The real $H_R(x)$ and imaginary $H_I(x)$ parts of $H(x)$ are shown in Figure 4.2. Using the spectrum symmetry, H_R was reflected to $[-0.5, 0]$ as an even function. Its graph is shown in Figure 4.3. Superimposed is a 8^{th} degree periodic polynomial continuation $\mathcal{C}\{H_R(x)\}$ with $b = 2$. An FFT/IFFT procedure using equation (4.10) is applied to $\mathcal{C}\{H_R(x)\}$ to compute its Hilbert transform $\mathcal{H}[\mathcal{C}\{H_R(x)\}]$ and reconstruct H_I. The result is depicted in Figure 4.4 together with the original $H_I(x)$, $x \in [0, 0.5]$. For comparison, we also show the Hilbert transform of $H_R(x)$ computed using MatLab built-in function *hilbert* that uses the same FFT/IFFT procedure but without periodic continuation. Clearly the reconstruction $\mathcal{H}[\mathcal{C}\{H_R(x)\}]$ of $H_I(x)$ using the

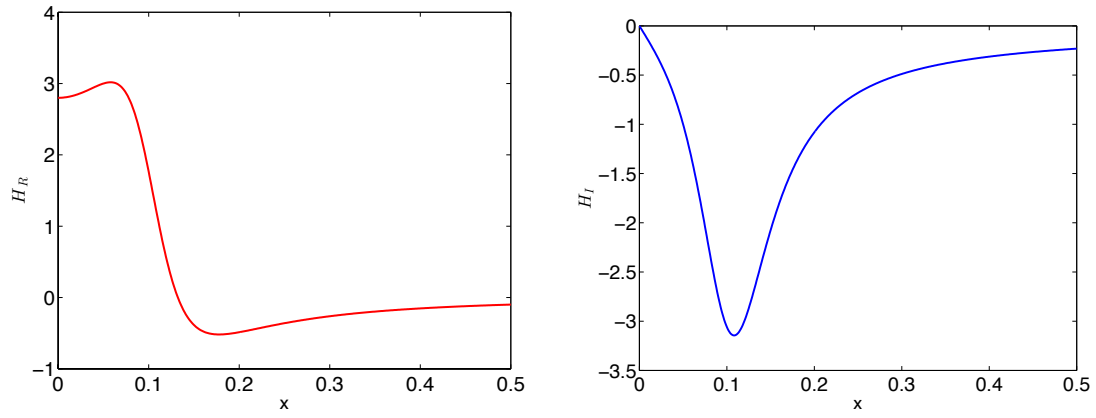

Figure 4.2: Study Case I: $H_R(x)$ and $H_I(x)$, $x \in [0, 0.5]$.

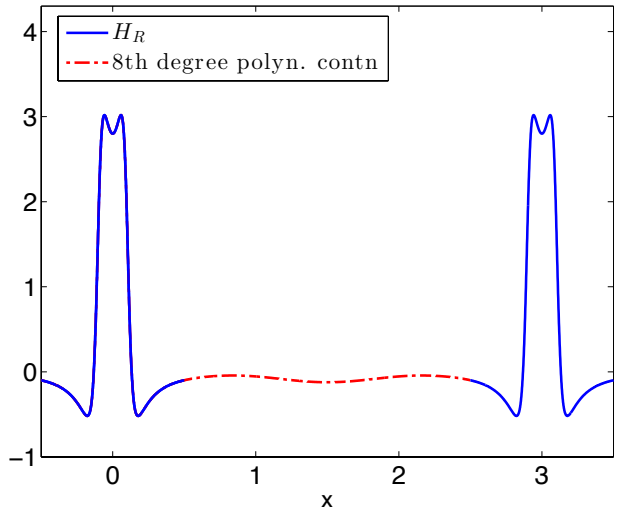

Figure 4.3: Study Case I: $H_R(x)$ and its periodic 8th degree polynomial continuation $\mathcal{C}[H_R](x)$.

periodic polynomial continuation defined in (4.11) is very close to the original H_I on $[0, 0.5]$, whereas MatLab built-in function *hilbert* produces large boundary errors.

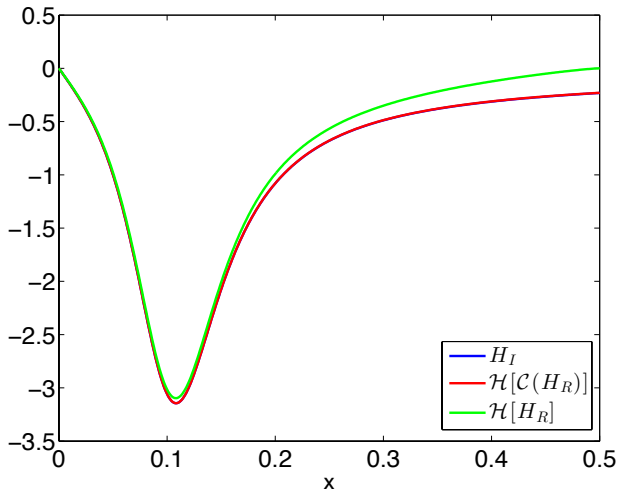

Figure 4.4: Study Case I: $H_I(x)$ vs. $\mathcal{H}[\mathcal{C}\{H_R(x)\}]$ and $\mathcal{H}[H_R(x)]$ computed using MatLab built-in function *hilbert* (with no continuation).

In Figure 4.5 we plot the absolute error E_C between $H_I(x)$ and its reconstruction using polynomial periodic continuations of degrees $p = 2$, 4, 6 and 8. We can see that the error, especially in the boundary regions, decreases as the degree of the polynomial increases, though not monotonically in this example. For comparison, we also plot the error E with using MatLab function *hilbert* that does not use periodic continuation. We can see that this error is about 5 times larger than that with the polynomial continuation of degree $p = 2$ and 100 times larger than with 8^{th} degree polynomial continuation. Figure 4.6 shows the error E_C with using 8^{th} degree polynomial continuation. This error is at most $2 \cdot 10^{-3}$ in the boundary regions and smaller away from the boundary. Hence, we clearly see that using polynomial continuation decreases the boundary errors and the smoother continuation is, the smaller reconstruction error is.

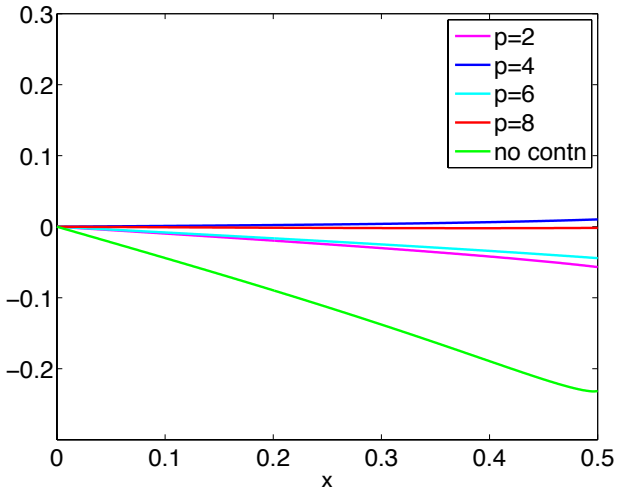

Figure 4.5: Study Case I: Error E_C with polynomial continuations of degree $p = 2$, 4, 6, 8 superimposed with the error E with no continuation.

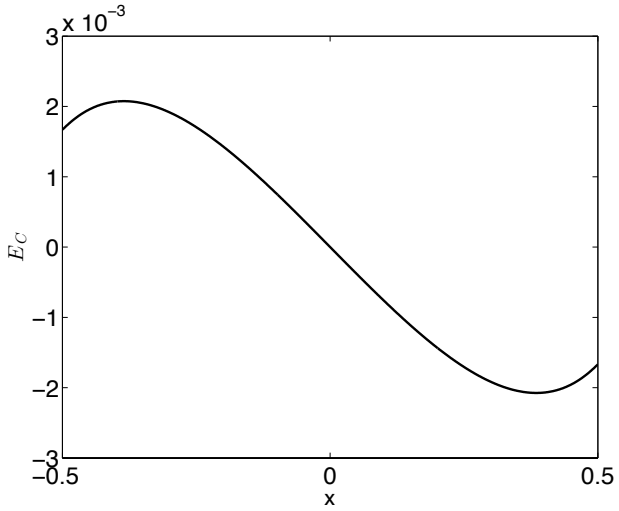

Figure 4.6: Study Case I: Error E_C using 8^{th} degree polynomial continuation and $b = 2$.

4.3.2 Study Case II: Transmission Line Transfer Function

In this study case we use the polynomial continuation method to verify causality of a uniform transmission line transfer function. The transmission line segment under test has the following per-unit-length parameters: $L = 4.73$ nH/cm, $C = 3.8$ pF/cm, $R = 0.8$ Ω/cm, $G = 0$ and length $\mathcal{L} = 10$ cm. The set of frequency points used to construct the discrete transfer function is sampled from the interval $(0, 5.0]$ GHz. This

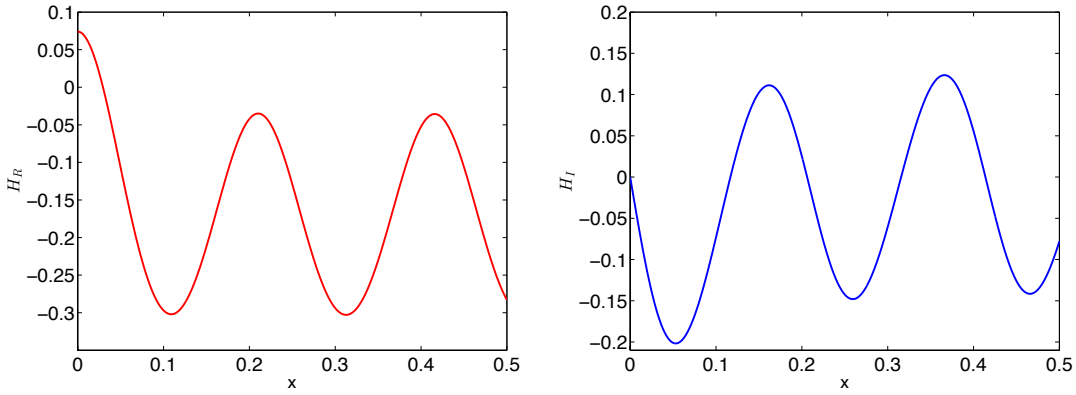

Figure 4.7: Study Case II: Real and imaginary parts of $H(x)$.

example was used in [67] to analyze causality using generalized dispersion relations with subtractions. The scattering matrix S of the structure was computed using MatLab function *rlgc2s*. Then we consider the element $H(w) = S_{11}(w)$. Due to limitation of the model used in the MatLab function *rlgc2s*, we can not obtain the value of the transfer function at $w = 0$ but we can sample it from any small nonzero frequency $w_{min} > 0$. However, the value of $H(w)$ at $w = 0$ is finite, so we have bandpass case. Again, we rescale the frequency interval to $(a, 0.5]$. We know that the $H_I(w)$ equals 0 at $w = 0$ due to odd symmetry of H_I. Since H_R is an even function, we have its values on $[-0.5, -a]$. The missing values of H_R in $[-a, a]$ can be approximated by constructing an even degree polynomial defined in (4.14). The real and imaginary parts of $H(x)$ are shown in Figure 4.7. H_R together with its 8^{th} degree polynomial continuation $\mathcal{C}\{H_R(x)$ are presented in Figure 4.8. Figure 4.9 shows H_I,

its reconstruction $\mathcal{H}[\mathcal{C}\{H_R(x)\}]$ and $\mathcal{H}[\{H_R(x)\}]$ without periodic continuation. The absolute errors E_C and E are presented in Figure 4.10.

Results indicate that polynomial continuation allows one to reduce the error inside the original interval by at least two orders of magnitude and around one order of magnitude at the boundary. Even though the error in the boundary region depends primarily on the order of polynomial continuation and not so much on the mesh frequency size, the accuracy in reconstruction in the region near $x = 0$ depends on resolution. As the number N of samples increases, thus, w_{min} decreases, the error in reconstruction near $x = 0$ also decreases as a function of N. We experimented with N ranging from 70 to 2000. The logarithmic graph plotted in Figure 4.11 shows that for small N, the error decreases as a function of N^{-3}, while for large values it behaves as $1/N$.

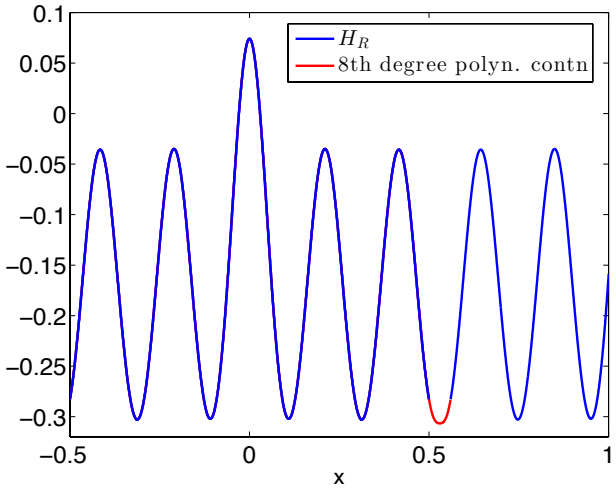

Figure 4.8: Study Case II: $H_R(x)$ and its periodic polynomial continuation.

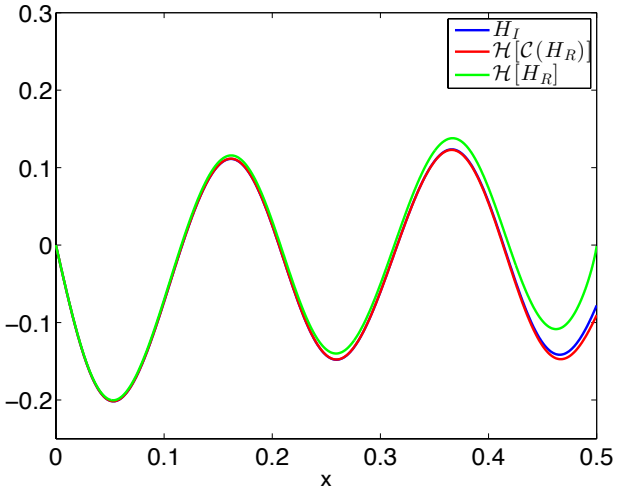

Figure 4.9: Study Case II: $H_I(x)$ vs. $\mathcal{H}[\mathcal{C}\{H_R(x)\}]$ and $\mathcal{H}[H_R(x)]$.

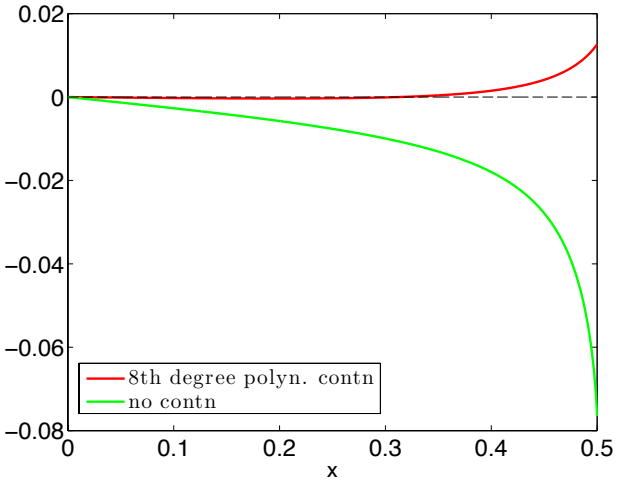

Figure 4.10: Study Case II: Errors E_C with 8th degree polynomial continuation and E (with no continuation).

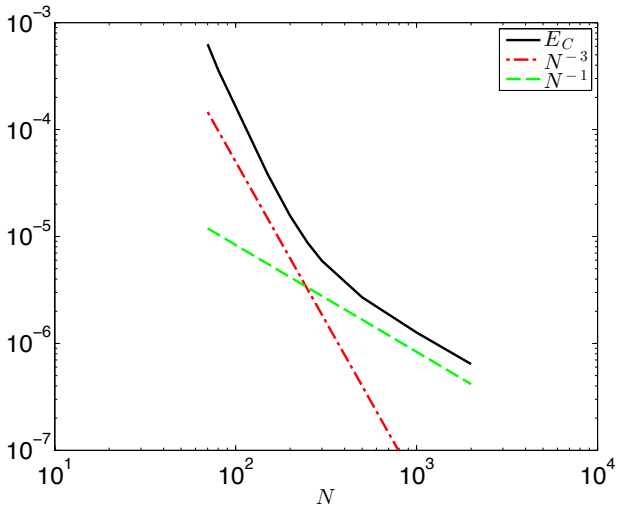

Figure 4.11: Error E_C near $x = 0$ as a function of N with 8th degree polynomial continuation.

Next we artificially impose a localized causality violation modeled by a Gaussian function

$$a \exp\left(-\frac{(x-x_0)^2}{2\sigma^2}\right), \quad 6\sigma = 10^{-2},$$

where a and x_0 are an amplitude and location of a perturbation. A symmetric perturbation is imposed at $-x_0$. The results with $x_0 = 0.1$, $a = 10^{-2}$, 10^{-3} and 10^{-4} are shown in Figure 4.12. We note that the approach with a polynomial periodic continuation give superior results over the approach without a continuation. While for larger amplitude $a = 10^{-2}$ both methods allow to detect the causality violation, the method with continuation maintains much smaller error away from the region where the violation was imposed while when there is no continuation, the error is not small essentially everywhere. When $a = 10^{-3}$, the approach with continuation detects successfully the violation, while the error with the method without continuation produces spikes in the error similar to the approach with continuation but the error at the spikes and around is quite away from zero and about the same magnitude, so in this case (without continuation) it not possible to distinguish causality violation from the reconstruction error. With even smaller amplitude $a = 10^{-4}$, the approach

with a polynomial continuation is still able to detect causality violation by developing spikes in the reconstruction error but these spikes are of about the same magnitude as the rest of the surrounding error, so in such a case causality error is indistinguishable from the reconstruction error. If no continuation is used, the results are even worse.

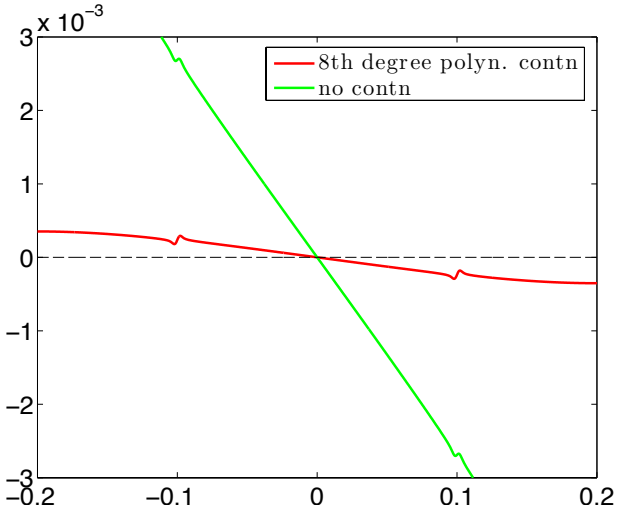

Figure 4.12: Study Case II: Error E_C with imposed causality violation with amplitude $a = 10^{-2}$ using 8^{th} degree polynomial continuation and the error E without any continuation used.

4.3.3 Study Case III: DDRAM Package Macromodel

This study case uses a scattering S-matrix of a DRAM package with 110 input and output ports, which was generated by a Finite Element Method. The values of the scattering matrix are available at $N = 100$ equally spaced frequency points ranging from w_{min}=0 to $w_{max} = 5$ GHz. We apply the technique to the S-parameter $H(w) = S(100, 1)$ that relates the output signal from port 100 to the input signal at port 1 as a function of frequency w. The procedure can be extended to other elements of S by applying the method to every element of the scattering matrix. After rescheduling frequencies to $[-0.5, 0.5]$ we obtain function $H(x)$. The real and imaginary parts of $H(x)$ is plotted in Figure 4.13.

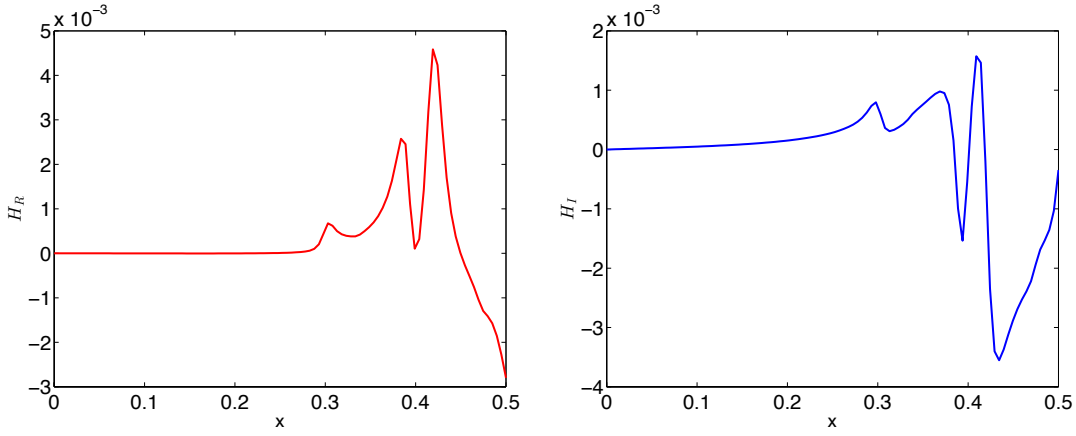

Figure 4.13: Study Case III: Real and imaginary parts of $H(x)$.

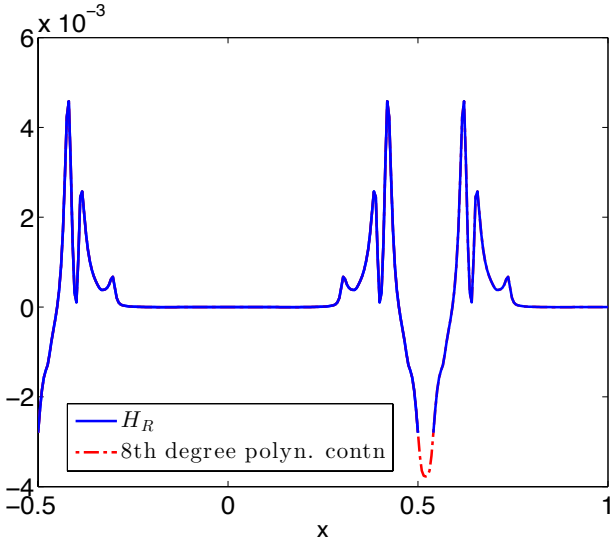

Figure 4.14: Study Case III: $H_R(x)$ and its periodic 8th degree polynomial continuation with $b = 0.2$.

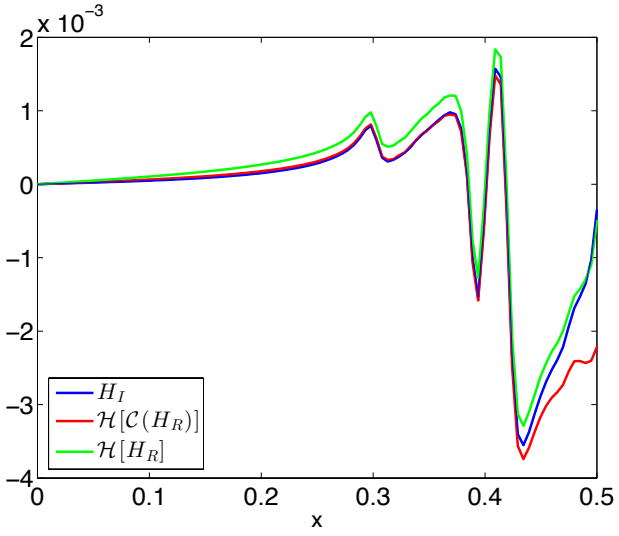

Figure 4.15: Study Case III: $H_I(x)$ vs. $\mathcal{H}[\mathcal{C}\{H_R(x)\}]$ and $\mathcal{H}[\{H_R(x)\}]$.

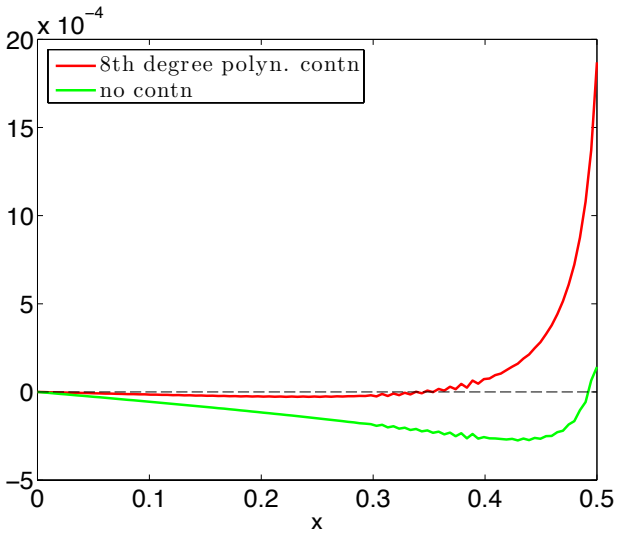

Figure 4.16: Study Case III: Errors E_C with 8th degree polynomial continuation and E (with no continuation).

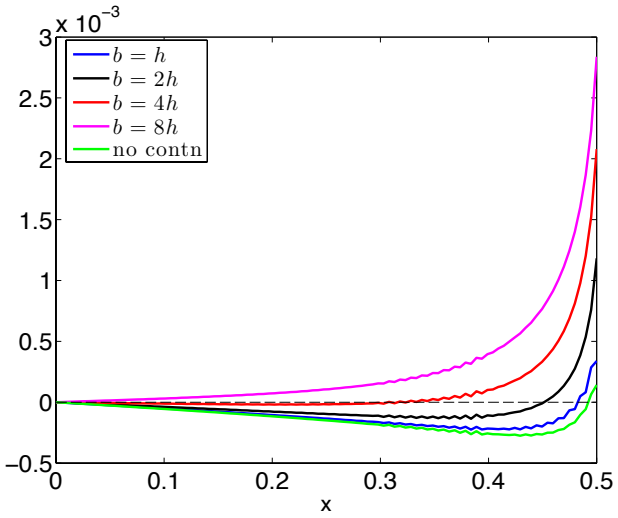

Figure 4.17: Study Case I: Error E_C with 8th degree polynomial continuation and b varying from $b = 0$ (no continuation) and $b = h$, $2h$, $4h$ and $8h$.

Figures 4.14 shows $H_R(x)$ together with its 8^{th} degree polynomial continuation $\mathcal{C}\{H_R(x)\}$ and $b = 0.2$. The Hilbert transform of the continued function $\mathcal{H}[\mathcal{C}\{H_R(x)\}]$ is illustrated in Figure 4.15. For comparison, we also show $\mathcal{H}[\{H_R(x)\}]$ is no periodic continuation was used. The absolute errors E_C and E are presented in Figure 4.16.

The results indicate that periodic continuation allows one to maintain a small uniform error (on the order of 10^{-5}) away from the boundary unlike the approach without continuation that produces the error of by about two orders of magnitude bigger. However, the error at the boundary in this example is bigger with $b > 0$ compared to $b = 0$. This can be explained by the fact that both $H_R(x)$ and $H_I(x)$ have steep slopes at the end points that are most likely signs of a discontinuity that is typical for transfer functions of real life high speed interconnects. In Figure 4.17 we analyze the absolute error of reconstruction of $H_I(x)$ as a function of the length b of the extended domain. As b increases from $b = 0$ to $b = 8h$ with $h = 0.0051$, we observe that the error away from the boundary decreases and reaches its minimum (optimal value) around $b = 4h$ and then starts to increase. The error at the boundary increases monotonically with b.

Chapter 5

Causality Verification and Enforcement via SVD-Based Fourier Continuations

5.1 Introduction

A new method, presented in this Chapter, is an alternative approach for causality verification and enforcement. This approach is based on Fourier continuation of a transfer function $H(w)$ under investigation. The discrete data of the transfer function are typically available only on a finite bandwidth. These data are not periodic in general. Direct application of dispersion relations in equations (3.8) and (3.9) using Fast Fourier Transform produces significant errors in the boundary regions mainly because if the values of $H(w)$ at endpoints are not the same, the transfer function is treated as discontinuous periodic function with the discontinuity at endpoints. To overcome this difficulty, we construct a spectrally accurate periodic continuation of $H(w)$ in an extended domain using the truncated singular value decomposition (SVD) method and impose causality directly on Fourier coefficients. A method for constructing a periodic continuation, also known as Fourier continuation or Fourier extension, based on regularized singular value decomposition (SVD), is proposed in [77]-[80]. This method allows one to calculate Fourier series approximations of non-periodic functions such that a Fourier series is periodic in an extended domain. The Fourier coefficients need to be determined by solving an overdetermined or underdetermined and regularized least square problem since the system suffers from numerical ill-conditioning. Fourier continuation based SVD was studied further in [81]-[83] and used to construct efficient algorithms for the numerical solution of linear [84], and nonlinear partial differential equations [85]-[87]. In [88], the SVD-based Fourier continuation method has

been extended to unevenly spaced data. Sobolev smoothed Fourier continuations are proposed in [89] where the approach allows one to construct dramatically smoothed Fourier continuation in the sense that the Fourier coefficients exhibit a prescribed rate of decay as the wave number increases. The smoothing does not significantly affect the accuracy of the Fourier series approximations on the original interval and may even yield better accuracy than the standard regularized SVD-based Fourier continuation.

Once the Fourier series is written for the Fourier continuation, the causality conditions are imposed directly on the Fourier coefficients producing a causal Fourier continuation. After computing the Fourier coefficients, the Fourier continuation is reconstructed and the resulting causal periodic continuations are then compared with the given discrete data on the original bandwidth of interest and a decision about whether the given data is causal or not is made depending on an error threshold.

The chapter is organized as follows. In Section (5.2) we derive causal spectrally accurate Fourier continuation using singular value decomposition (SVD). We also discuss the effect of using Sobolev smoothing proposed in [89]. In Section (5.3), the technique is applied to several analytic and simulated causal and non-causal examples to analyze performance of the method.

5.2 Causal Fourier Continuation

In practice, the transfer function is obtained either from numerical computations or direct measurements, and it is available only at a set of discrete frequencies in the range $[w_{min}, w_{max}]$, where $w_{min} \geq 0$. We first consider the baseband case when $w_{min} = 0$. Since equations (3.8) and (3.9) are homogeneous in the frequency variable we can rescale $[0, w_{max}]$ to $[0, 0.5]$ using the transformation $x = 0.5/w_{max}$ as we did in Chapter 4.

As we discussed in Chapter 4, the time domain impulse function $h(t)$ is often

real-valued. In this case, the real and imaginary parts of $H(w)$ are even and odd functions, respectively. This implies that the values of the transfer function $H(w)$ are available on the interval $x \in [-0.5, 0.5]$ by spectrum symmetry, so that the discrete set of rescaled frequencies is contained in the unit length interval. In some cases, the data is available only from a non-zero, low-frequency cutoff, i.e. the data window is $[w_{min}, w_{max}]$, where $w_{min} > 0$, which corresponds to the bandpass case. For example, in optical experiments, only a part of the electromagnetic spectrum is accessible [90].

The new procedure can be generalized to the bandpass case as well. The idea is to construct an accurate Fourier series approximation of $H(w)$ by allowing the Fourier series to be periodic and causal in an extended domain. The result is the Fourier continuation of $H(w)$ that we denote by $C_F(H(w))$, and it is defined by

$$\mathcal{C}_F(H(x)) = \sum_{k=-M/2+1}^{M/2} \alpha_k \, \mathrm{e}^{-\frac{2\pi i}{b} kx} \tag{5.1}$$

for even values of M, whereas when M is odd, the index k varies from $-\frac{M-1}{2}$ to $\frac{M-1}{2}$. Throughout this paper we will take M to be even for simplicity. All presented results have analogues for odd values of M. Here b is the period of approximation. Note that in the previous chapter on polynomial continuation, b denoted the length of the "added" region, not the entire period. For SVD-based periodic continuations b is normally chosen as twice the length of the domain on which function $H(x)$ is given [79]. For causal Fourier continuations we find that b can be varied to get best results, ranging, for example, from $b = 1.1$ to $b = 10$. It is assumed that the function $H(x)$ is known at N discretization points $\{x_j\}$, $j = 1, \cdots, N$, $x \in [-0.5, 0.5]$. Note that $C_F(H(x))$ is a trigonometric polynomial of degree at most $M/2$.

Since $H_R(x)$ and $H_I(x)$ are even and odd functions of x, respectively, the Fourier

coefficients α_k are real, where

$$\alpha_k = \frac{1}{b}\int_{-b/2}^{b/2} H(x)\overline{\phi_k(x)}dx, \quad j = 1, \ldots, M$$

and $^-$ denotes the complex conjugate.

Functions $\phi_k(x) = \mathrm{e}^{-\frac{2\pi i k x}{b}}$, $k \in \mathbb{Z}$, are orthogonal and, in particular,

$$\int_{-b/2}^{b/2} \phi_k(x)\overline{\phi_{k'}(x)}dx = b\,\delta_{kk'}$$

where $\delta_{kk'}$ is the Kronecker delta. In addition $\overline{\phi_k}(x) = \mathrm{e}^{\frac{2\pi i k x}{b}} = \phi_{-k}(x)$. For a function e^{-iax}, $a > 0$, the Hilbert transform is

$$\mathcal{H}\{\mathrm{e}^{-iax}\} = i\,\mathrm{sgn}(a)\,\mathrm{e}^{-iax},$$

hence, for function $\phi_k(x) = \mathrm{e}^{\frac{-2\pi i}{b}kx}$, we have

$$\mathcal{H}\{\mathrm{e}^{\frac{-2\pi i}{b}kx}\} = i\,\mathrm{sgn}(k)\cdot\mathrm{e}^{\frac{-2\pi i}{b}kx}$$

i.e

$$\mathcal{H}\{\phi_k(x)\} = i\,\mathrm{sgn}(k)\phi_k(x). \tag{5.2}$$

This implies that the functions $\{\phi_k(x)\}$ are the eigenfunctions of the Hilbert transform (HT) with associated eigenvalues $\pm i$. We use relations (5.2) to impose causality conditions on the coefficients of $\mathcal{C}_F(H(x))$. We can write $\mathcal{C}_F(H(x))$ as a Fourier series

$$\mathcal{C}_F(H(x)) = \sum_{k=-\infty}^{\infty} \alpha_k\phi_k(x)$$

We will truncate this series at the end to get a Fourier continuation in the form (6.1).

Let

$$\mathcal{C}_F(H(x)) = \mathrm{Re}\{\mathcal{C}_F(H(x))\} + j\,\mathrm{Im}\{\mathcal{C}_F(H(x))\}$$

and

$$\phi_k(x) = \mathrm{Re}\{\phi_k(x)\} + j\,\mathrm{Im}\{\phi_k(x)\}.$$

Since

$$\mathrm{Re}\{\phi_k(x)\} = \frac{1}{2}(\phi_k(x) + \overline{\phi_k(x)})$$

and

$$\mathrm{Im}\{\phi_k(x)\} = \frac{1}{2i}(\phi_k(x) - \overline{\phi_k(x)})$$

we obtain

$$\mathrm{Re}\{\mathcal{C}_F(H(x))\} = \sum_{k=-\infty}^{\infty} \alpha_k\,\mathrm{Re}\{\phi_k(x)\} = \frac{1}{2}\sum_{k=-\infty}^{\infty} \alpha_k(\phi_k(x) + \overline{\phi_k(x)})$$

and, since $\overline{\phi_k(x)} = \phi_{-k}(x)$ we have

$$\mathrm{Re}\{\mathcal{C}_F(H(x))\} = \frac{1}{2}\sum_{k=-\infty}^{\infty} \alpha_k(\phi_k(x) + \phi_{-k}(x)).$$

By changing the order of summation, we obtain

$$\mathrm{Re}\{\mathcal{C}_F(H(x))\} = \frac{1}{2}\sum_{k=-\infty}^{\infty} (\alpha_k + \alpha_{-k})\phi_k(x).$$

Similarly, the imaginary part

$$\mathrm{Im}\{\mathcal{C}_F(H(x))\} = \sum_{k=-\infty}^{\infty} \alpha_k\,\mathrm{Im}(\phi_k(x)) = \frac{1}{2i}\sum_{k=-\infty}^{\infty} \alpha_k(\phi_k(x) - \overline{\phi_k(x)})$$

and, since $\overline{\phi_k(x)} = \phi_{-k}(x)$ we have

$$\mathrm{Im}\{\mathcal{C}_F(H(x))\} = \frac{1}{2i}\sum_{k=-\infty}^{\infty} \alpha_k(\phi_k(x) - \phi_{-k}(x))$$

and after changing the order of summation we get

$$\mathrm{Im}\{\mathcal{C}_F(H(x))\} = \frac{1}{2i}\sum_{k=-\infty}^{\infty} (\alpha_k - \alpha_{-k})\phi_k.$$

For a causal periodic extension, we need $\mathrm{Im}\{\mathcal{C}_F(H(x))\}$ to be the Hilbert transform of $-\mathrm{Re}\{\mathcal{C}_F(H(x))\}$. Hence,

$$\frac{1}{2i}\sum_{k=-\infty}^{\infty} (\alpha_k - \alpha_{-k})\phi_k(x) = -\mathcal{H}\left[\frac{1}{2}\sum_{k=-\infty}^{\infty} (\alpha_k + \alpha_{-k})\phi_k(x)\right].$$

Using linearity of the Hilbert transform, we get

$$\frac{1}{2i}\sum_{k=-\infty}^{\infty} (\alpha_k - \alpha_{-k})\phi_k(x) = -\frac{1}{2}\sum_{k=-\infty}^{\infty} (\alpha_k + \alpha_{-k})\mathcal{H}\{\phi_k(x)\}.$$

Using (5.2), we can write

$$\frac{1}{2i}\sum_{k=-\infty}^{\infty} (\alpha_k - \alpha_{-k})\phi_k(x) = -\frac{1}{2}\sum_{k=-\infty}^{\infty} (\alpha_k + \alpha_{-k})i\,\mathrm{sgn}(k)\phi_k(x).$$

Hence, we obtain

$$\frac{1}{2i}(\alpha_k - \alpha_{-k}) = -\frac{1}{2}(\alpha_k + \alpha_{-k})i\,\mathrm{sgn}(k) \quad \text{for any } k \in \mathbb{Z}$$

or

$$\alpha_k - \alpha_{-k} = (\alpha_k + \alpha_{-k})\,\mathrm{sgn}(k), \quad k \in \mathbb{Z}$$

that implies $\alpha_k = 0$ for $k < 0$. Hence, the Fourier continuation (6.1) can be written

as

$$\mathcal{C}_F(H(x)) = \sum_{k=0}^{\infty} \alpha_k \phi_k(x)$$

Hence, the Fourier continuation (5.1) can be written as

$$\mathcal{C}_F(H(x)) = \sum_{k=0}^{M/2} \alpha_k \phi_k(x), \tag{5.3}$$

where we truncated the infinite sum to obtain a trigonometric polynomial. Evaluating $H(x)$ at points x_j, $j = 1, \ldots, N$, $x_j \in [-0.5, 0.5]$ produces a complex valued system

$$\mathcal{C}(H)(x_j) = \sum_{k=0}^{M/2} \alpha_k \phi_k(x_j) \tag{5.4}$$

with N equations for $M/2+1$ unknowns α_k, $k = 1, \ldots, M/2+1$. Separating the real and imaginary parts, we get

$$\begin{aligned} \operatorname{Re}(\mathcal{C}_F(H(x_j))) &= \sum_{k=0}^{M/2} \alpha_k \operatorname{Re}(\phi_k(x_j)), \\ \operatorname{Im}(\mathcal{C}_F(H(x_j))) &= \sum_{k=0}^{M/2} \alpha_k \operatorname{Im}(\phi_k(x_j)). \end{aligned} \tag{5.5}$$

To ensure that the Fourier coefficients α_k are real, instead of solving system of equations (5.4), one can solve the system (5.5). This produces $2N$ equations (N equations for real parts and N equations for imaginary parts) and unknowns α_k. Typically the system is overdetermined and has to be solved in the least squares sense. We also consider the case of the underdetermined system when the number of data samples $2N$ is less than the number of Fourier coefficients $M/2+1$. Introduce the following notation:

$\vec{f} = \big(\operatorname{Re} H(x_1), \ldots, \operatorname{Re} H(x_N), -\operatorname{Im} H(x_1), \ldots, -\operatorname{Im} H(x_N)\big)^T$

$\vec{\alpha} = \big(\alpha_0, \ldots, \alpha_{M/2}\big)$

and introduce matrix A whose entries are:

$$A_{jk} = \mathrm{Re}\{\mathrm{e}^{\frac{-2\pi i}{b}kx_j}\} \quad \text{for } j = 1, \ldots, N,\ k = 0, \ldots, M/2$$

$$A_{(j+N),k} = \mathrm{Im}\{\mathrm{e}^{\frac{-2\pi i}{b}kx_j}\} \quad \text{for } j = 1, \ldots, N,\ k = 0, \ldots, M/2.$$

Then the coefficients α_k, $k = 1, \ldots, N$, are defined as a least-squares solution that minimizes the Euclidean norm of the residual:

$$\min_{\{\alpha_k\}} \sum_{j=1}^{2N} \left| \sum_{k=0}^{M/2} \alpha_k A_{jk} - f_j \right|^2 \tag{5.6}$$

This least-squares problem is extremely ill-conditioned, as explained in [81] using the theory of frames. However, it can be regularized using a truncated SVD method when singular values below some tolerance ξ close to the machine precision are being discarded. It was shown that this approach produces very accurate solutions for evenly spaced points [77, 79, 83] or even unstructured grids [79].

In this work we use $\xi = 10^{-13}$ as the threshold to filter the singular values. The ill-conditioning increases as M increases by developing rapid oscillations in the extended region. These oscillations are typical for SVD-based Fourier continuations. Once the system reaches a critical size that does not depend on the function being approximated, the coefficient matrix becomes rank deficient and the regularization of the SVD is required to treat singular values close to the machine precision. Because of the rank deficiency, the Fourier continuation is no longer unique. Applying directly the SVD method produces the minimum norm solution $\{\alpha_k\}$, $k = 1, \ldots, M/2 + 1$, i.e. the set of Fourier coefficients whose Euclidean norm is minimized, for which the corresponding Fourier continuation is oscillatory. The oscillations in the extended region do not affect significantly the causality of the Fourier continuation and we show that varying the length of the extended domain helps in reducing the effect of

high gradient regions on the error between the given data and causal continuation on the original interval.

Another way to have some control on the Fourier coefficients of the continuation is to use a Sobolev smoothing technique proposed in [89]. It allows one to compute corrections β_k to the Fourier coefficients α_k, so that the modified Fourier series (the smoothed Fourier continuation) $C_s(H(x))$ become:

$$\mathcal{C}_S(H(x)) = \sum_{0}^{M/2} (\alpha_k + \beta_k)\, \mathrm{e}^{\frac{-2\pi i}{b} kx} \tag{5.7}$$

is smoothed by taking into account the contribution of each Fourier coefficient to the H^p Sobolev norm of the Fourier continuation but maintains the accuracy of the original Fourier continuation with using only α_k given by (6.24). Coefficients β_k are computing using the discarded singular values, i.e the singular values $\sigma_k < \xi$, and the corresponding right singular vectors from the null space of matrix A [89]. The effect of including the coefficients β_k in the Fourier continuation can be seen by looking at the magnitudes of the coefficients of the smoothed Fourier continuation $C_S(H)$ compared with the Fourier coefficients of the original $\mathcal{C}_F(H)$. While the magnitudes of the Fourier coefficients of $\mathcal{C}_F(H)$ barely decays at all, the coefficients of the smoothed function $C_S(H)$ decay quickly, at the rate of $\mathcal{O}(|k|^{-p})$. The effect of the smoothing is proportional to the filter level ξ.

5.3 Numerical Experiments: Causality Verification

In this section we employ the causal spectral continuation method to verify causality of the same test functions used in the previous chapter where the polynomial continuation method was developed and applied to characterize causality, as well as analyze other functions.

5.3.1 Study Case I: Two-pole Transfer Function

In this study case the new approach is applied on a system with two-pole transfer function [91] with the time delay $T_o = 0$. The transfer function is defined by

$$H(w) = \frac{r}{iw + P} + \frac{\overline{r}}{iw + \bar{P}} \tag{5.8}$$

where $r = 1 + 3i$, $P = 1 + 2i$, so the poles of this function are in the upper half plane at $\pm 2 + i$. Therefore, the transfer function is causal as a linear combination of causal transforms. We sample data on the interval from $w = 0$ to $w_{max} = 6$, use the spectrum symmetry to obtain data on $[-w_{max}, 0)$ and scale the frequency interval from $[-w_{max}, w_{max}]$ to $[-0.5, 0.5]$ by using substitution $x = 0.5w/w_{max}$. The real and imaginary parts of $H(x)$ plotted on $[-0.5, 0.5]$ are shown in Figures 5.1 and 5.2. Superimposed there are their causal Fourier continuations obtained using $M = 500$, $N = 1000$ and $b = 4$ and solving the complex system (5.4) and its real counterpart (5.5). As can be seen, there is no essential difference in using complex or real formulation. The data and the causal Fourier continuations are essentially undistinguishable on $[-0.5, 0.5]$.

Denote by E_R and E_I the absolute errors in the reconstruction of $H_R(x)$ and $H_I(x)$, respectively:

$$E_R(x) = \operatorname{Re} H(x) - \operatorname{Re} \mathcal{C}(H)(x), \qquad E_I(x) = \operatorname{Im} H(x) - \operatorname{Im} \mathcal{C}(H)(x).$$

We find that in this example both errorsE_R and E_I are at the order of 10^{-14}.

In Figures 5.3 and 5.4 we plot the real and imaginary part of the data together with their causal Fourier continuations using the same $M = 500$, $N = 1000$, $b = 6$ in the extended domain to show the nature of these continuations. It is obvious that the continuations oscillate in the extended region outside $[-0.5, 0.5]$. The frequency

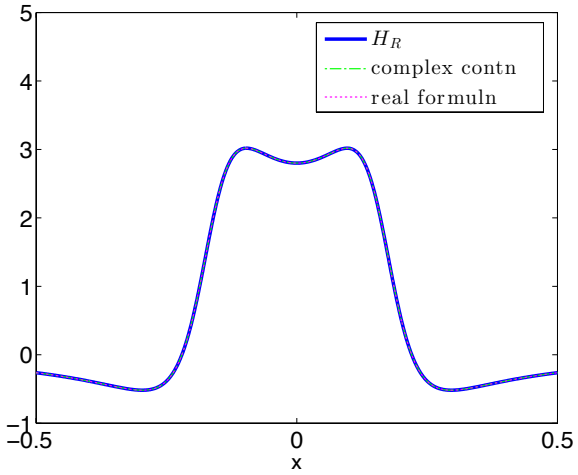

Figure 5.1: Study Case I: $H_R(w)$ and its Fourier continuation with $M = 500$, $N = 100$, $b = 4$ shown on $[-0.5, 0.5]$.

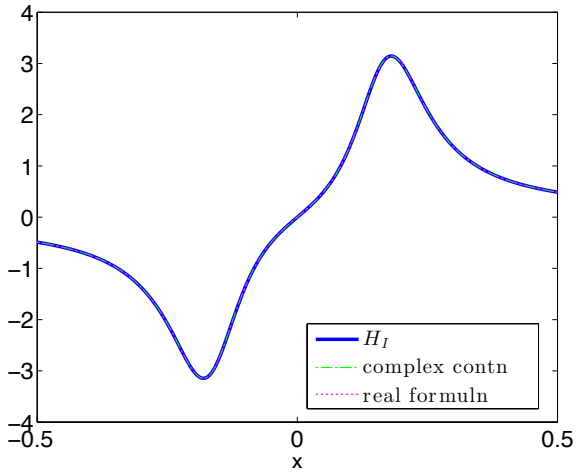

Figure 5.2: Study Case I: $H_I(w)$ and its Fourier continuation with $M = 500$, $N = 100$, $b = 4$ shown on $[-0.5, 0.5]$.

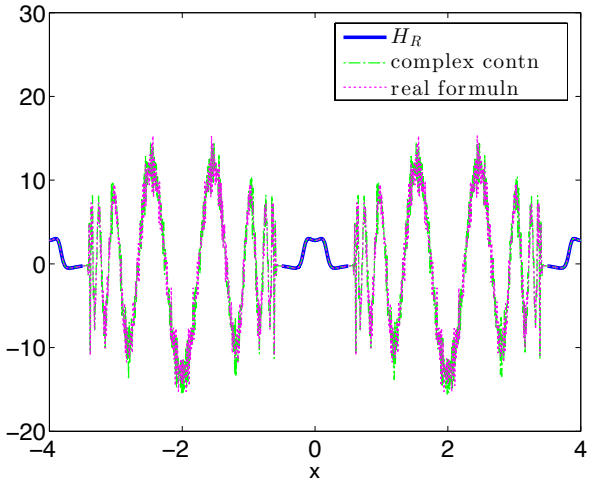

Figure 5.3: Study Case I: Fourier continuation of $H_R(w)$ with $M = 500$, $N = 1000$, $b = 6$.

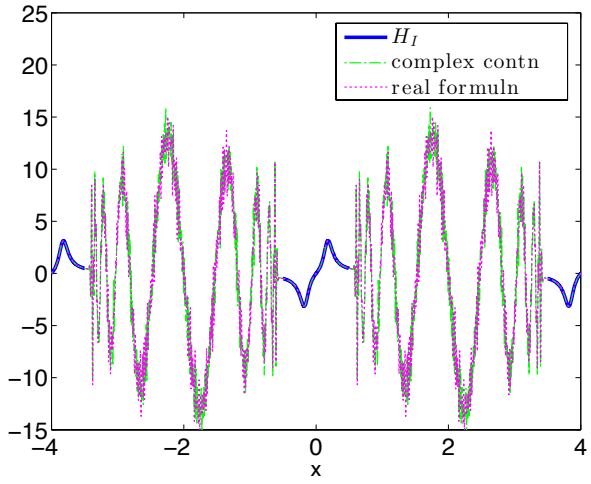

Figure 5.4: Study Case I: Fourier continuation of $H_I(w)$ with $M = 500$, $N = 1000$, $b = 6$.

of these oscillations increases with M. At the same time, continuations become more and more accurate in approximations in the original interval $[-0.5, 0.5]$.

In Figures 5.5 and 5.6 we plot the errors E_R and E_I in the original region $[-0.5, 0.5]$ for various values of M. As M increases from $M = 10$ to $M = 100$, the order of the error decreases from 10^{-1} to 10^{-14} for both real and imaginary parts. The errors E_R and E_I for $M = 500$, $N = 1000$, $b = 6$ are presented in Figures 5.7 and 5.8.

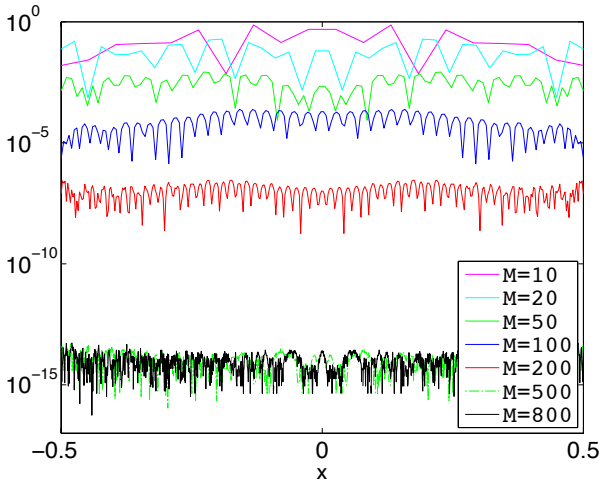

Figure 5.5: Study Case I: Semilogy plot of the error $E_R(x)$ on the original scaled frequency interval $[-0.5, 0.5]$ with $M = 10$, 20, 50, 100, 200 and 500, $N = 2M$, $b = 4$.

The above results demonstrate that the method is capable of verifying causality of causal functions with the accuracy close to the machine precision.

Next we alter the causal data by adding a small non-causal perturbation

$$P(x) = a \exp\left(-\frac{(x - x_0)^2}{2\sigma^2}\right), \quad a = 10^{-10}, \quad \sigma = 10^{-2}/6 \tag{5.9}$$

to $H_R(x)$ and demonstrate that the proposed method is capable of detecting such violation of causality. The perturbation is a Gaussian function centered at $x_0 = 0.1$ with an amplitude of $a = 5 \cdot 10^{-13}$ and standard deviation $10^{-2}/6$, so its effect is concentrated on the interval of length 10^{-2} and outside this interval the values of this

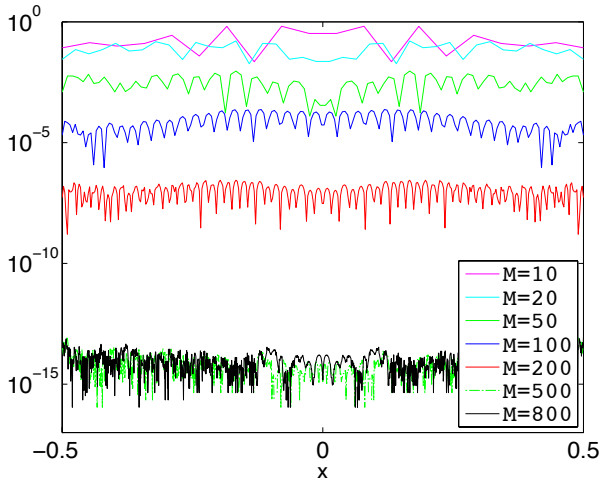

Figure 5.6: Study Case I: Semilogy plot of the error $E_I(x)$ on the original scaled frequency interval $[-0.5, 0.5]$ with $M = 10$, 20, 50, 100, 200 and 500, $N = 2M$, $b = 4$.

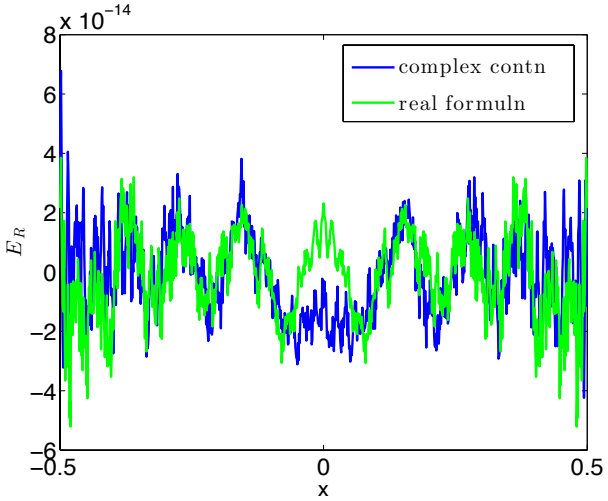

Figure 5.7: Study Case I: Semilogy plot of the error $E_R(x)$ on the original scaled frequency interval $[-0.5, 0.5]$ with $M = 500$, $N = 1000$, $b = 4$.

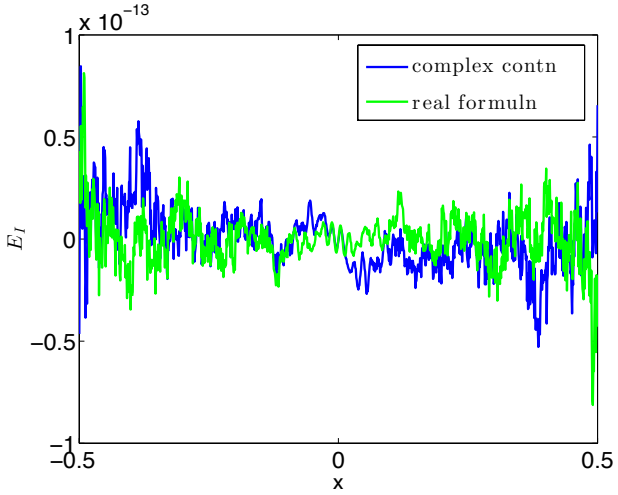

Figure 5.8: Study Case I: Semilogy plot of the error $E_I(x)$ on the original scaled frequency interval $[-0.5, 0.5]$ with $M = 500$, $N = 1000$, $b = 4$.

perturbation are very small and close to 0. The amplitude of the added perturbation is much smaller (by 10^{-13}) compared with the magnitude of H_R and H_I of the original data (the maximum values of H_R and H_I are about 3.5 and 6, respectively). The errors E_R and E_I are shown in Figures 5.9 and 5.10. It is clear that the errors have spikes at $x = \pm 0.1$ due to symmetry that corresponds to the location of Gaussian perturbations. The amplitude of these spikes is of the order of 10^{-13}, whereas the rest of the error has magnitude 10^{-14}, i.e. 10 times smaller than in the perturbation regions.

For larger perturbation, the results are similar. For example, with $a = 10^{-8}$, the error at $x = \pm 0.1$ is of the order of 10^{-9} and the rest of the interval has the error about 10 times smaller. If $a = 10^{-6}$, the spikes in the error at $x = \pm 0.1$ are of the order of 10^{-7} and the rest is of 10^{-8} as shown in Figures 5.11 and 5.12.

Effect of Lower Number of Data Points

It is not always possible to sample data with a desired frequency step. In certain cases, one is given a discrete set of data of fixed size N. But M is a free parameter that can be varied. When N is fixed and M varies, the systems (5.4) or (5.5) may

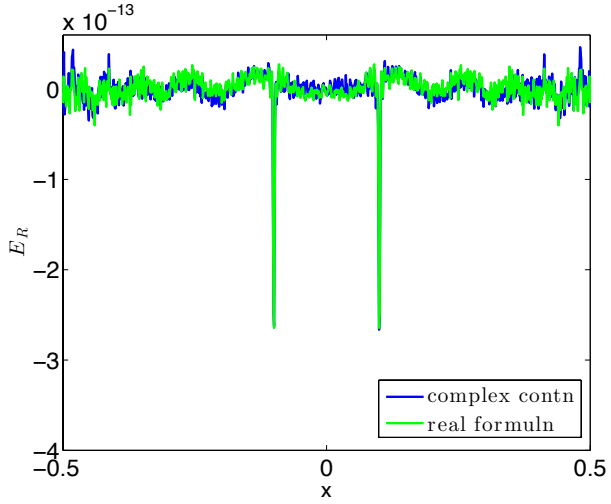

Figure 5.9: Study Case I: Error E_R when a non-causal perturbation with $a = 5 \cdot 10^{-13}$ is added, $M = 500$, $N = 1000$, $b = 4$.

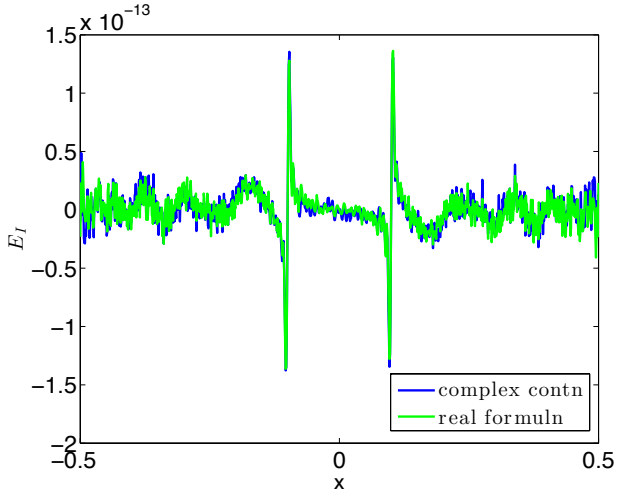

Figure 5.10: Study Case I: Error E_I when a non-causal perturbation with $a = 5 \cdot 10^{-13}$ is added, $M = 500$, $N = 1000$, $b = 4$.

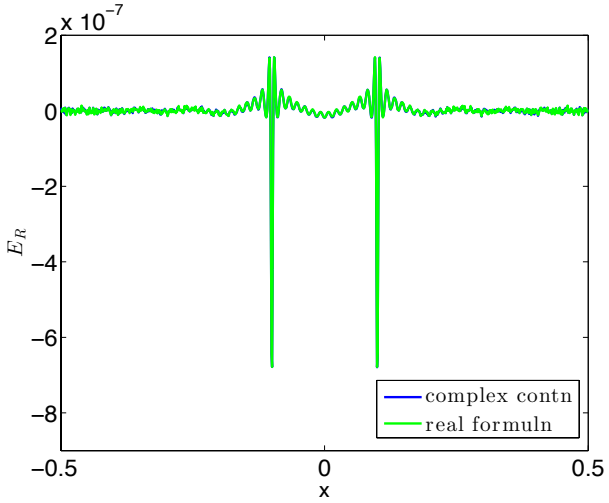

Figure 5.11: Study Case I: Error E_R when a non-causal perturbation with $a = 10^{-6}$, $M = 500$, $N = 1000$, $b = 4$.

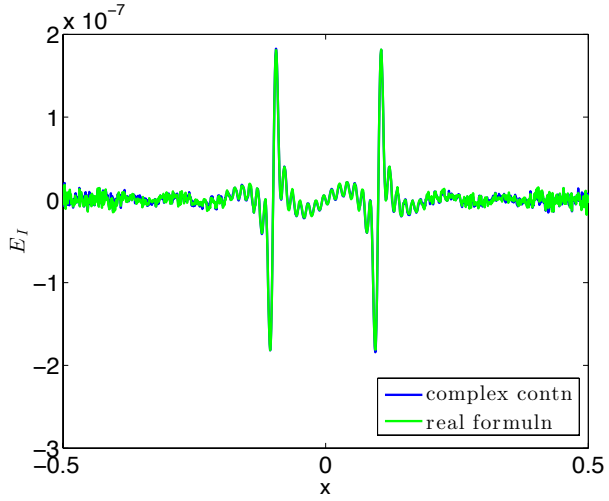

Figure 5.12: Study Case I: Error E_I when a non-causal perturbation with $a = 10^{-6}$, with $M = 500$, $N = 1000$, $b = 4$.

become underdetermined. We show that in these cases it is still possible to compute accurate minimum norm least squares solution. With the same function as above, we fix $M = 500$ and analyze the l_∞ norms of errors E_R and E_I in reconstructing $H_R(x)$ and $H_I(x)$ when M is fixed and N decreases from $N = 2M$ to $N = M/10$ on the original interval $[-0.5, 0.5]$. This is equivalent of having fixed N and increase M. The results are shown in Table 5.1. They indicate that both errors slightly decrease as N uncreases. We also find that as N decreases, the Fourier continuation become less

M	N	$\|\|E_R\|\|_\infty$	$\|\|E_I\|\|_\infty$
500	$2M = 1000$	$5.2069 \cdot 10^{-14}$	$8.1268 \cdot 10^{-14}$
500	$M = 500$	$4.835 \cdot 10^{-14}$	$4.452 \cdot 10^{-14}$
500	$M = N/2 = 250$	$6.3394 \cdot 10^{-14}$	$6.3838 \cdot 10^{-14}$
500	$M = N/5 = 100$	$2.5979 \cdot 10^{-14}$	$2.8422 \cdot 10^{-14}$
500	$M = N/10 = 50$	$6.8834 \cdot 10^{-15}$	$3.5527 \cdot 10^{-15}$

Table 5.1: Study Case I: Errors E_R and E_I with fixed number of Fourier coefficients M and decreasing number N of data samples.

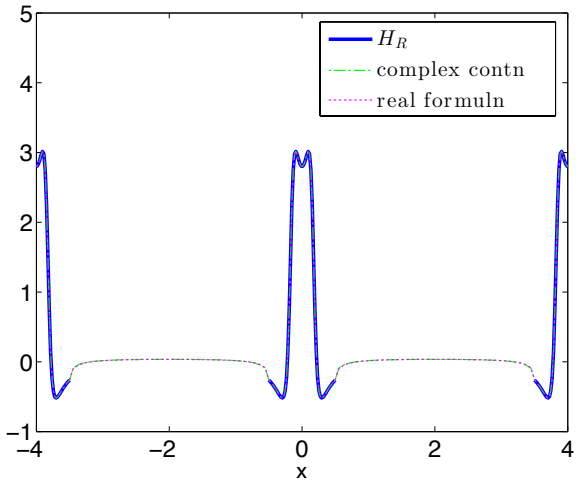

Figure 5.13: Study Case I: $H_R(w)$ and its Fourier continuation with $M = 500$, $N = M/10 = 50$, $b = 4$.

oscillatory and it does not oscillate at all for $N = M/10$ as can be seen in Figures 5.13 and 5.14. The singular values do not decay to 0 but instead slowly decay from 19.7990 to a constant value 14.

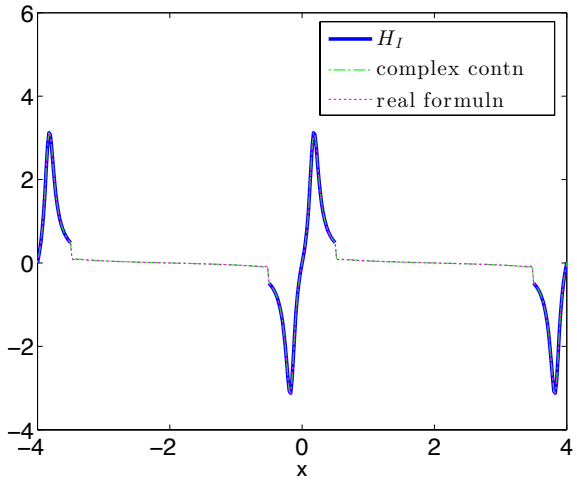

Figure 5.14: Study Case I: $H_I(w)$ and its Fourier continuation with $M = 500$, $N = M/10 = 50$, $b = 4$

5.3.2 Study Case II: DDRAM Package Macromodel

The second study case is an S-parameter data set that was generated through a Finite Element Modeling (FEM) of a DRAM package considered in Section 4.3.3. Here we use $H(w) = S(100, 1)$ and scale it to $H(x)$ defined on $[0, 0.5]$ as before. The number of the data points is fixed at $N = 100$, so to construct a causal Fourier continuation we can only vary the number of Fourier coefficients M and the length of the extended region b. Computing a causal Fourier continuation with $M \leq N$ does not give the required accuracy and as the error can not be made smaller than 10^{-4}. Therefore, we try increasing the number of Fourier coefficients M while keeping the number of sample points N fixed. This corresponds to the under-sampling of the Fourier transform but it is found to be very effective in signal processing. Because of the symmetry, the number of data points is $2N - 1 = 199$. We choose to use $b = 1.1$. Slightly higher values of b give similar results while using too large b does not produce small enough error. This is most likely because the resolution becomes lower with using a larger domain and the fixed number of points. We vary values of M from 100 to 500 and find that the error decreases from 10^{-4} with $M = 100$ to 10^{-8} with

$M = 400$ and becomes very small at the order of 10^{-18} with $M = 500$. The details are shown in Table 5.2.

M	$\|\|E_R\|\|_\infty$	$\|\|E_I\|\|_\infty$
100	$1.5 \cdot 10^{-4}$	$2 \cdot 10^{-4}$
200	$1.5 \cdot 10^{-5}$	$1 \cdot 10^{-5}$
300	$8 \cdot 10^{-7}$	$1 \cdot 10^{-6}$
400	$5 \cdot 10^{-8}$	$8 \cdot 10^{-8}$
500	$8 \cdot 10^{-18}$	$8 \cdot 10^{-18}$

Table 5.2: Study Case II: Errors E_R and E_I with $N = 100$, $b = 1.1$ and M varying from 100 to 500.

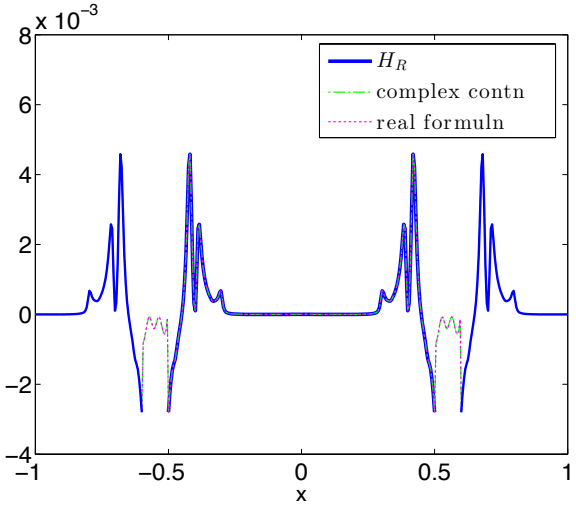

Figure 5.15: Study Case II: $H_R(x)$ and its Fourier continuation with $M = 500$, $N = 100$, $b = 1.1$.

In Figures 5.15 and 5.16 we plot $H_R(x)$ and $H_I(x)$ together with their causal Fourier continuations obtained with $M = 500$ and $b = 1.1$. The errors E_R and E_I on the original interval are on the order of 10^{-18} and are plotted in Figures 5.17 and 5.18, respectively.

5.3.3 Study Case III: Transmission Line Transfer Function

We consider a uniform transmission line segment with per-unit-length parameters $L = 4.73$ nH/cm, $C = 3.8$ pF/cm, $R = 0.8$ Ω/cm, $G = 0$ and length $\mathcal{L} = 10$

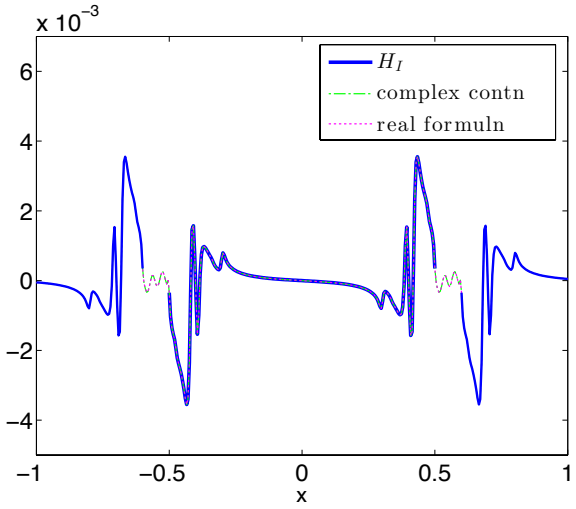

Figure 5.16: Study Case II: $H_I(x)$ and its Fourier continuation with $M = 500$, $N = 100$, $b = 1.1$.

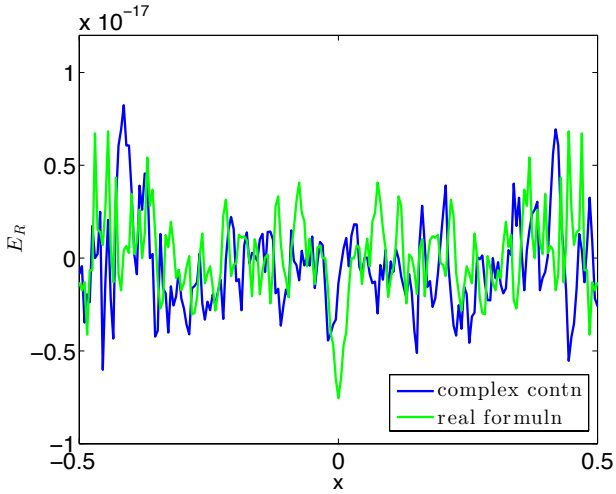

Figure 5.17: Study Case II: Error $E_R(x)$ with $M = 500$, $N = 100$, $b = 1.1$.

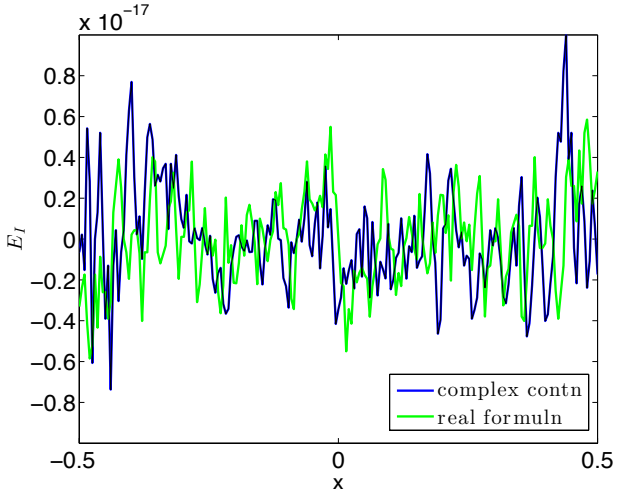

Figure 5.18: Study Case II: Error $E_I(x)$ with $M = 500$, $N = 100$, $b = 1.1$.

cm. The frequency is sampled from the interval $(w_{min}, 5.0]$ GHz. This example was studied in Section 4.3.2. We use the element $H(w) = S_{11}(w)$. As was explained in that section, we can not obtain the value of the transfer function at $w = 0$ but we can sample it from any small nonzero frequency $w_{min>0}$ that we choose to be the mesh size $h = w_{max}/N$ in our data. Using spectrum symmetry we reflect the values of the transfer function for negative frequencies. We know that the $H_I(0) = 0$ since H_I is an odd function but $H_R(0)$ is unknown. For this reason, our frequencies at which the values of the transfer function are available have a gap at $w = 0$. Nevertheless, our approach is still applicable since it does not require the data points to be equally spaced. Alternatively, we can use a polynomial interpolation to find a value of $H_R(w)$ at $w = 0$ as was done in Section 4.3.2. The value of the imaginary part $H_I(0) = 0$ by symmetry. This second approach is not very accurate since it does not take into account causality when the polynomial interpolation of $H_R(w)$ for small w is constructed, and produces a larger error compared with just skipping the values at $w = 0$. As before, we rescale the transfer function to $H(x)$, $x \in (0, 0.5]$. Using our spectral continuation technique with $w_{max} = 5.0$ GHz, $M = N = 3000$ and $b = 4$ we are able to construct a causal Fourier continuation accurate within $3 \cdot 10^{-15}$.

The graphs of $H_R(x)$ and $H_I(x)$ together with their causal Fourier continuations are presented in Figures 5.19and 5.20. The corresponding reconstruction errors E_R and E_I on the original interval is shown in Figures 5.21 and 5.22.

With smaller values of w_{max}, it is enough to use smaller values of M and N to get the same order of accuracy. For example, to get an error in approximation of the transfer function on the original interval at the order of 10^{-14} and $w_{max} = 3.0$ GHz, it is enough to use $M = N = 1500$, while for $w_{max} = 1$ GHz one could use $M = N = 500$. This can be explained by the fact that when the number M of Fourier coefficients increases, the least squares problem (3.16) or (3.17) to compute Fourier coefficients becomes more ill-conditioned and the effect of round-off errors increases. Moreover, with smaller N we get regularization by discretization and fewer Fourier coefficients are required.

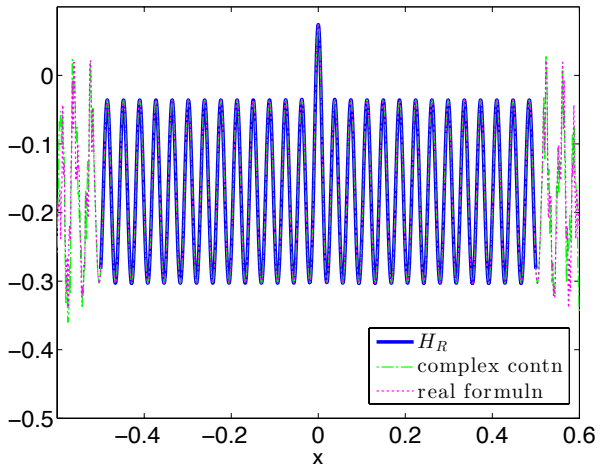

Figure 5.19: Study Case III: $H_R(x)$ and its causal Fourier continuation with $M = N = 3000$, $b = 4$.

To verify the capability of the spectral continuation method to detect non-causality, we perturb the real part of $H(x)$, as in Study Case I, by a Gaussian function $\varepsilon \exp\left(-\frac{(x-x_0)^2}{2\sigma^2}\right)$ centered at $x_0 = 0.1$, with amplitude $\varepsilon = 10^{-6}$ and standard deviation $\sigma = 10^{-2}/6$, so that the perturbation is localized to approximately $(0.1 - 10^{-2}, 0.1 + 10^{-2})$. A symmetric perturbation is placed at $x = -0.1$. The error

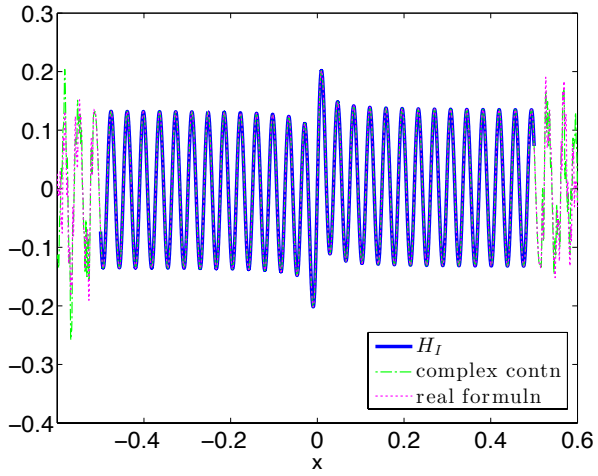

Figure 5.20: Study Case III: $H_I(x)$ and its causal Fourier continuation with $M = N = 3000$, $b = 4$.

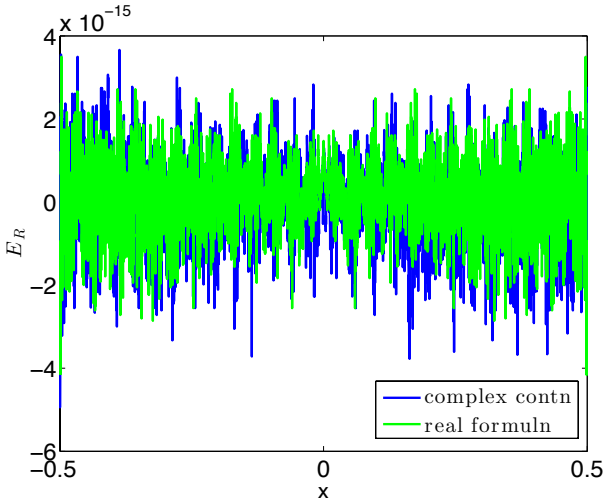

Figure 5.21: Study Case III: Error $E_R(x)$ with $M = N = 3000$, $b = 4$.

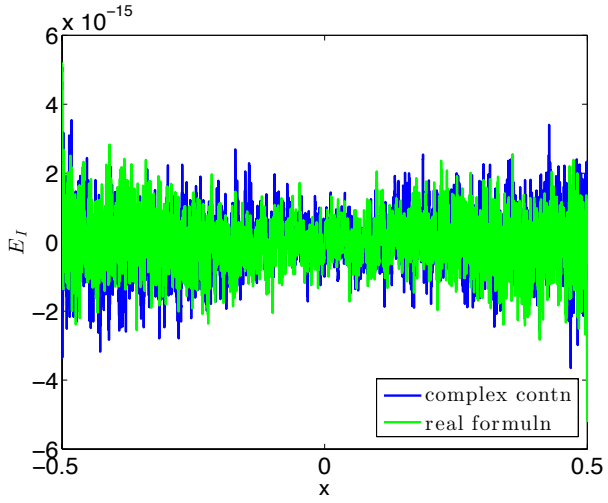

Figure 5.22: Study Case III: Error $E_I(x)$ with $M = N = 3000$, $b = 4$.

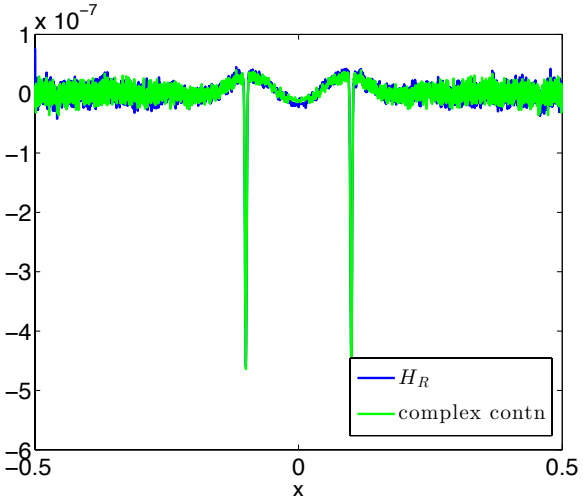

Figure 5.23: Study Case III: Error $E_R(w)$ with $M = N = 3000$, $b = 4$ with non-casual Gaussian perturbation with $\varepsilon = 10^{-6}$.

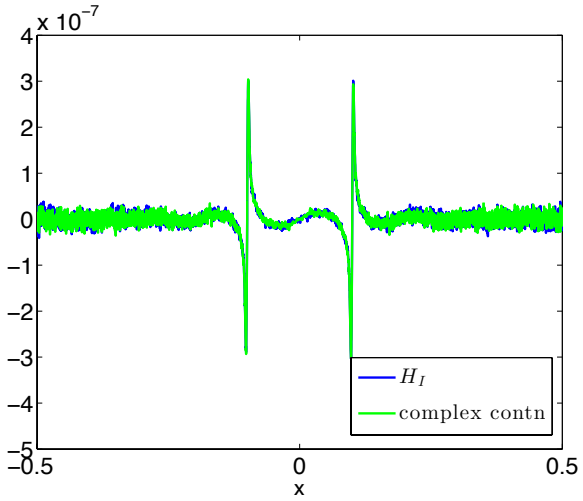

Figure 5.24: Study Case III: Error $E_I(x)$ with $M = N = 3000$, $b = 4$ and non-casual Gaussian perturbation with $\varepsilon = 10^{-6}$.

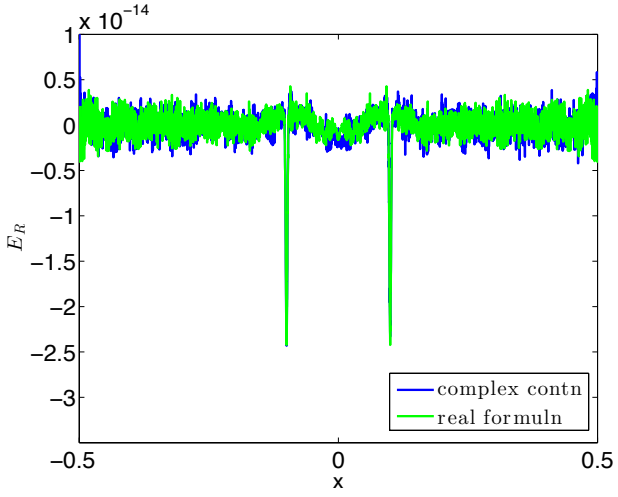

Figure 5.25: Study Case III: Error $E_R(x)$ with $M = N = 3000$, $b = 4$ and non-casual Gaussian perturbation with $\varepsilon = 5 \cdot 10^{-13}$.

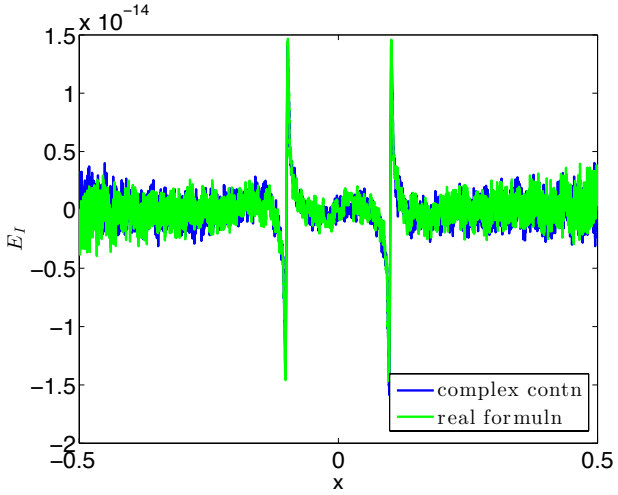

Figure 5.26: Study Case III: Error E_I with $M = N = 3000$, $b = 4$ and non-casual Gaussian perturbation with $\varepsilon = 5 \cdot 10^{-13}$.

in approximation with causal Fourier continuation is shown in Figures and (5.24. We can see very pronounced spikes in both real and imaginary parts of $H(x)$ at $x = \pm 1$ with amplitude $4.5 \cdot 10^{-7}$ while the rest of the error is on the order of $2 \cdot 10^{-8}$, approximately one order smaller. We tested the method further by decreasing the amplitude ε of the non-causal perturbation to see how small causality violations we can detect. The results are summarized in Table 5.3 where ε was varied from 10^{-6} to 10^{-14}. We are able to detect a causality violation of amplitude up to $\varepsilon = 5 \cdot 10^{-13}$ and we show the errors for this case in Figures 5.25 and 5.26.

ε	$E_R(x)$ at $x = \pm 0.1$	$E_I(x)$ at $x = \pm 0.1$	Error on the rest of $[-0.5, 0.5]$
10^{-6}	$4.5 \cdot 10^{-7}$	$3 \cdot 10^{-7}$	$2 \cdot 10^{-8}$
10^{-7}	$4.5 \cdot 10^{-8}$	$3 \cdot 10^{-8}$	$2 \cdot 10^{-9}$
10^{-10}	$4.5 \cdot 10^{-11}$	$3 \cdot 10^{-11}$	$2 \cdot 10^{-12}$
10^{-13}	$4.5 \cdot 10^{-14}$	$3 \cdot 10^{-14}$	$3 \cdot 10^{-15}$
$5 \cdot 10^{-14}$	$2.5 \cdot 10^{-14}$	$1.5 \cdot 10^{-14}$	$3 \cdot 10^{-15}$
10^{-14}	$6 \cdot 10^{-15}$	$4 \cdot 10^{-15}$	$3 \cdot 10^{-15}$

Table 5.3: Study Case III: Error in reconstruction of $H_R(x)$ and $H_I(x)$ with $M = N = 3000$, $b = 4$ and Gaussian perturbation with amplitude varying from 10^{-6} to 10^{-14}.

5.3.4 Study Case IV: Delayed Gaussian Transfer Function

In this study case we test the performance of the spectral continuation method on an example of a delayed Gaussian function that was used in [68] to check causality of interconnects through minimum-phase and all-pass decomposition. We consider the impulse response function modeled by a Gaussian with the center of the peak at t_d and standard deviation σ:

$$h(t, t_d) = \exp\left[-\frac{(t - t_d)^2}{2\sigma^2}\right].$$

If $t_d = 0$, the Gaussian function $h(t, 0)$ is even, so it can not be causal. As t_d increases, the center of the peak moves to the right and for $t_d > 3\sigma$ the impulse response function $h(t, t_d)$ gradually becomes causal. The corresponding transfer function is

$$H(w, t_d) = \exp\left[-2(\pi w\sigma)^2 - 2i\pi w\, t_d\right]$$

which is a periodic function damped by an exponentially decaying function. We consider two regimes. One has a very small value of $t_d < 3\sigma$ to give an example of a non-causal function. In the second regime, the delay $t_d > 3\sigma$ to give a big enough decay of the Gaussian and make the transfer function $H(w, t_d)$ causal. We fix $b = 4$, $\sigma = 2$ and sample w from the interval $[0, 4 \cdot 10^8]$ Hz and consider first the case with $t_d = 0.1\sigma$. The real and imaginary parts of $H(w, t_d)$ are shown in Figures 5.27 and 5.28. The errors $E_R(x)$ and $E_I(x)$ are shown in Figures 5.29 and 5.30. As the results indicate, the error is on the order of 10^{-4} and varying b or M (smaller or larger) does not essentially affect the error, its order remains the same.

In the second case, we set $t_d = 6\sigma$, which should give a causal enough function. Its real and imaginary parts are shown in Figures 5.31 and 5.32 and the corresponding errors that drop to the order of $2 \cdot 10^{-15}$ are presented in Figures 5.33 and 5.34.

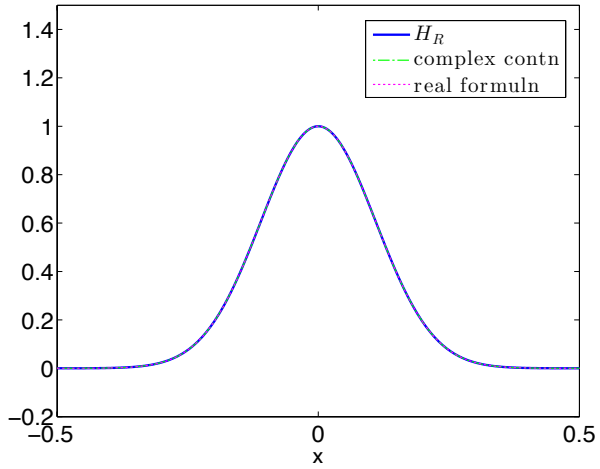

Figure 5.27: Study Case IV: $H_R(x)$ with its Fourier continuation with $M = N = 500$, $b = 4$, $t_d = 0.1\sigma$ in a non-causal case.

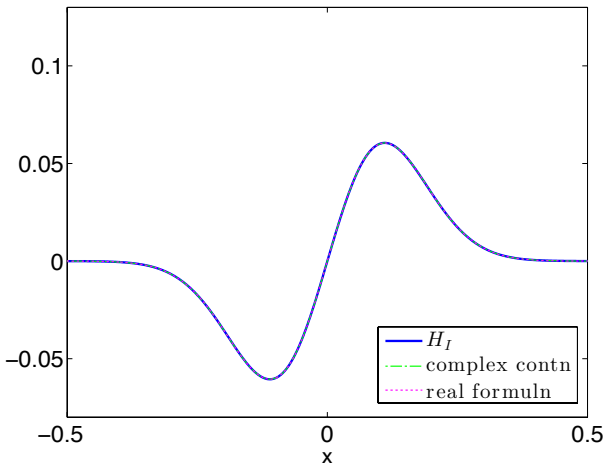

Figure 5.28: Study Case IV: $H_I(x)$ with its Fourier continuation with $M = N = 500$, $b = 4$, $t_d = 0.1\sigma$ in a noncausal case.

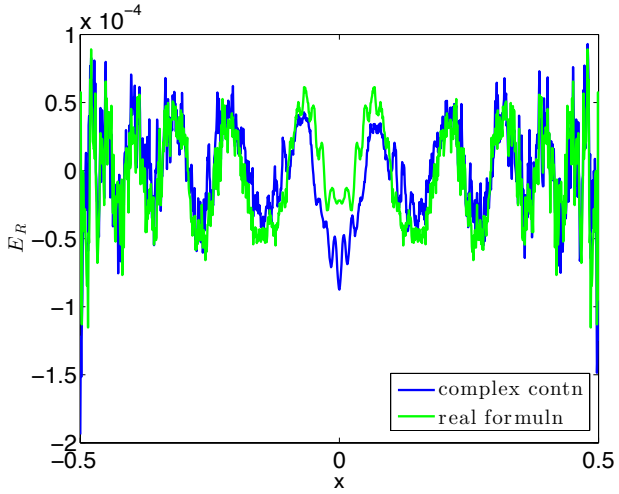

Figure 5.29: Study Case IV: $E_R(x)$ with $M = N = 500$, $b = 4$, $t_d = 0.1\sigma$ in a non-causal case.

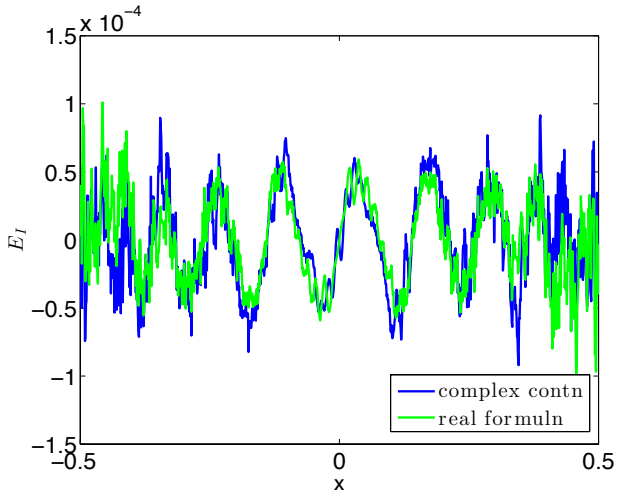

Figure 5.30: Study Case IV: $E_I(x)$ with $M = N = 500$, $b = 4$, $t_d = 0.1\sigma$ in a non-causal case.

We do observe a gradual change of the non-causal Gaussian function into a causal function. Making $t_d = \gamma\sigma$ and varying γ among 1, 2, 4, and 5, we find that the errors in approximation of the transfer function decay with γ and they are on the order of $5 \cdot 10^{-6}$, 10^{-7}, $3 \cdot 10^{-12}$ and 10^{-14}, respectively, as expected. Thus, this example also demonstrates an excellent performance of the new method.

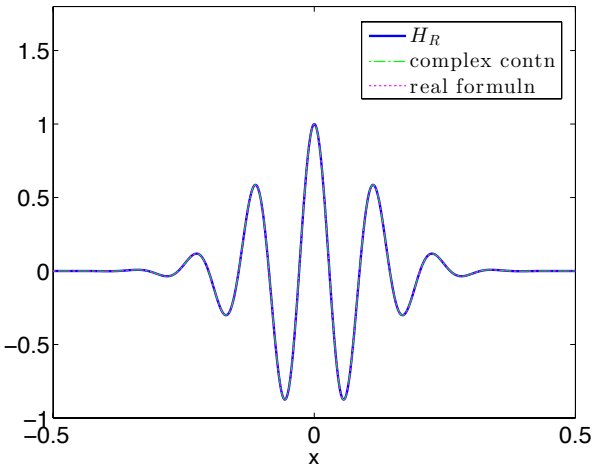

Figure 5.31: Study Case IV: $H_R(x)$ with its Fourier continuation with $M = N = 500$, $b = 4$, $t_d = 6\sigma$ in a causal case.

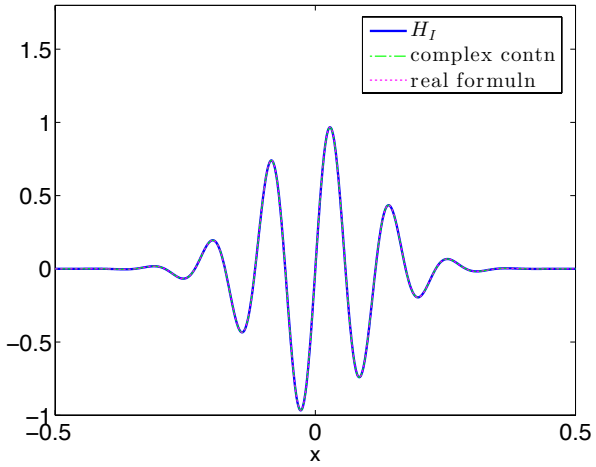

Figure 5.32: Study Case IV: $H_I(x)$ with its Fourier continuation with $M = N = 500$, $b = 4$, $t_d = 6\sigma$ in a causal case.

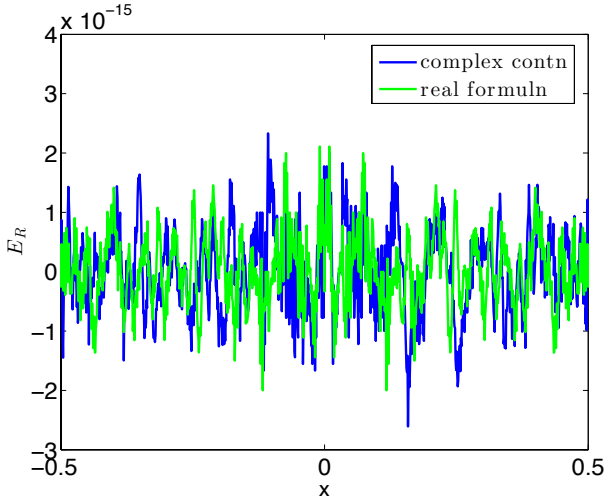

Figure 5.33: Study Case IV: $E_R(x)$ with $M = N = 500$, $b = 4$, $t_d = 6\sigma$ in a causal case.

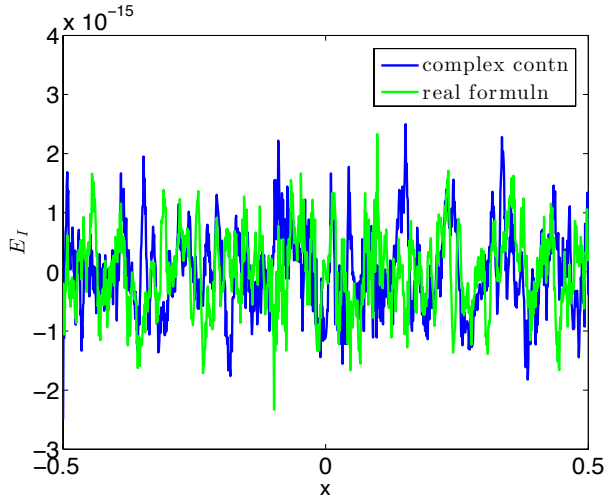

Figure 5.34: Study Case IV: $E_I(x)$ with $M = N = 500$, $b = 4$, $t_d = 6\sigma$ in a causal case.

Chapter 6

Conclusions

The design of high-speed interconnects, that are common on chip and at the package level in digital systems, requires systematic simulations at different levels in order to evaluate the overall electrical system performance and avoid signal integrity problems. To conduct such simulations, one needs suitable models that capture the relevant electromagnetic phenomena that affect the signal and power quality. These models are often obtained either from direct measurements or electromagnetic simulations in the form of discrete port frequency responses that represent scattering, impedance, or admittance transfer functions or transfer matrices in multidimensional cases, respectively. Once frequency responses are available, a corresponding macromodel can be derived using several techniques such as the Vector Fitting and the Orthonormal Vector Fitting among others. However, if the data are contaminated by errors, it may not be possible to derive a good model. These errors may be due to a noise, inadequate calibration techniques or imperfections of the test set-up in case of direct measurements or approximation errors due to the meshing techniques, discretization errors and errors due to finite precision arithmetic occurring in numerical simulations. Besides, these data are typically available over a finite frequency range as discrete sets with a limited number of samples. All this may affect the performance of the macromodeling algorithm resulting in non-convergence or inaccurate models. Often the underlying cause of such behavior is the lack of causality in a given set of frequency responses. A system is causal if a frequency response given by the transfer function $H(w)$ satisfies the dispersion relations also known as Kramers-Krönig relations. The dispersion relations characterize the causality in the frequency domain. They represent the fact that the real and imaginary parts of a causal function are related through Hilbert transform. The Hilbert transform may be expressed in both

continuous and discrete forms and is widely used in circuit analysis, digital signal processing, remote sensing and image reconstruction. The Hilbert transform that relates the real and imaginary parts of a transfer function $H(w)$ is defined on the infinite domain which can be reduced to $[0, \infty)$ by symmetry properties of $H(w)$ for real impulse response functions. However, the frequency responses are usually available over a finite length frequency interval, so the infinite domain is either truncated or behavior of the function for large w is approximated. This usually creates large errors in the boundary regions. The generalized dispersion relations or dispersion relations with subtractions can be used to increase the convergence of the dispersion integrals by making integrands less sensitive to the high-frequency behavior of $H(w)$, and, thus, reduce the reconstruction errors caused by the finite bandwidth.

We take another approach and instead of approximating the behavior of $H(w)$ for large w, truncating the domain or using the generalized dispersion relations with subtraction, we construct causal periodic polynomial and Fourier continuations of $H(w)$ by requiring the transfer function to be periodic and causal in an extended domain of finite length. The polynomial continuation approach allows the use of FFT/IFFT routines to compute discrete Hilbert transform and enforce causality in the frequency domain. The accuracy of the method is shown to depend primarily on the order of the polynomial, i.e. the degree of smoothness of the continuation at the end points of the given frequency domain. This in turn allows one to significantly reduce the boundary artifacts compared to the use of the function *hilbert* from the popular software Matlab that also implements discrete Hilbert transform but does not use any periodic continuation.

The second approach is also based on dispersion relations but it constructs SVD-based Fourier continuations. This is done by calculating accurate Fourier series approximations of transfer functions, not periodic in general, and allowing the Fourier series to be periodic in an extended domain. The causality is imposed directly on

Fourier coefficients using the Kramers-Krönig dispersion relations that require real and imaginary parts of the transfer function to be a Hilbert transform pair. This approach eliminates the necessity of approximating the behavior of the transfer function at infinity, which is known to be a source of significant errors in computation of the Hilbert transform defined on an infinite domain (or semi-infinite due to spectrum symmetry) with data available only on a finite bandwidth. In addition, this procedure does not require direct numerical computation of the Hilbert transform integral or using FFT/IFFT. The Fourier coefficients are computed by solving an oversampled or undersampled regularized least squares problem via a truncated SVD method to have the ill-conditioning of the system under control. Fourier continuations with the large number of Fourier coefficients are typically oscillatory in the extended domain but this does not essentially affect the quality of reconstruction and their effect can be minimized by varying the length of the extended domain.

Both methods are applicable to baseband and bandpass regimes and allow the user to verify causality and detect causality violations. They were tested on several analytic and simulated examples. While polynomial continuation method only reduces the boundary errors, the spectral continuation method is capable of eliminating boundary artifacts completely. It has much higher accuracy and can detect much smaller causality violations of the magnitude close to the machine precision.

References

[1] Bogatin, E., Signal Integrity: Simplified, Prentice Hall, 2003 Ed.

[2] Hall, S. H.; Hall, G. W.; McCall, J. A., High-Speed System Digital Design, New York: Wiley, 2000.

[3] Tummala, R., Fundamentals of Microsystems Packaging, McGraw Hill, 2001.

[4] Johnson, H.; Graham, M., High-Speed Digital Design, US; Prentice Hall PTR, 2003.

[5] Hall, S. H.; Hall, G. W.; McCall, J. A., High Speed Digital System Design - A Handbook of Interconnect Theory and Design Practice, John Wiley Sons, Inc. 2000.

[6] Granberg, T., Handbook of digital techniques for high speed design, in Prentice Hall Modern Semiconductor Design Series. Englewood Cliffs, NJ: Prentice-Hall, 2004.

[7] Veenstra, H.; and Long, J. R., Circuit and interconnect design for RF and high bit-rate applications, in Analog and Signal Processing, New York: Springer, 2008.

[8] International Technology Roadmap for Semiconductors Update Overview. (2009). [Online]. Available: http://www.itrs.net/

[9] Green, L., "Understanding the importance of signal integrity", Circuits and Devices Magazine, IEEE , vol. 15, no. 6, pp.7–10, Nov 1999.

[10] John Patrin, "An Overview of Signal Integrity," High-Performance System Design Conference, DesignCon 2003.

[11] Jiang Jing; Kong Lingwen, "Study of signal integrity for PCB level," 11th International Conference on Electronic Packaging Technology and High Density Packaging (ICEPT-HDP), pp.828–833, Aug. 2010.

[12] Swaminathan, M.; Ege Engin, A., "Modeling of Signal and Power Integrity in System on Package Applications," EMC 2007 IEEE International Symposium on Electromagnetic Compatibility, pp.1–6,July 2007.

[13] Baek, H.; Eisenstadt, W.R., "Signal integrity characterization of high-speed I/O in 3D chip-package system," 2013 IEEE 14th Annual Wireless and Microwave Technology Conference (WAMICON), pp.1–4, April 2013.

[14] Zuowei Shen; Jian Tong, "Signal Integrity Analysis of High-Speed Single-Ended and Differential Vias", EPTC 2008. 10th Electronics Packaging Technology Conference, pp.65–70, Dec. 2008.

[15] Rahman, T.; Yan, Z.; Abubakar, I., "Signal integrity for high speed digital design," 9th International Symposium on Antennas Propagation and EM Theory (ISAPE), pp.1113–1115, Nov. 2010.

[16] Cuny, R., "SPICE and IBIS Modeling kits The Basis for Signal Integrity Analysis" IEEE International Symposium on Electromagnetic Compatibility, pp. 204–208, 1996.

[17] Rangaswamy, G.; Prathaban, S., "Signal Integrity Analysis with Power Delivery Network," 2006. IEEE Workshop on Signal Propagation on Interconnects, pp.205–207, May 2006.

[18] Tuckley, K.R.; Pinto, R.P., "Signal integrity consideration in high density digital Signal Processing boards," 10th International Conference on Electromagnetic Interference and Compatibility INCEMIC, pp.113–117, Nov. 2008.

[19] Nagpal, R.; Malik, R.; Tripathi, J., "Signal Integrity and Power Integrity Methodology for Robust Analysis of On-the-Board System for High Speed Serial Links," 12th Euromicro Conference on Digital System Design, Architectures, Methods and Tools, DSD '09, pp.742–745, Aug. 2009.

[20] Erden Motoglu et al, "Statistical Signal Integrity Analysis and Diagnosis Methodology for High-Speed Systems", IEEE Transactions on Advanced Packaging, Vol. 27, No. 4, Nov. 2004.

[21] "Designing for Signal Integrity with Advanced Design System", Agilent EEs of EDA, 13 May 2008.

[22] Ryu, W. H.; Wang, M., "A Co-Design Methodology of Signal Integrity and Power Integrity", High-Performance System Design Conference, DesignCon 2006.

[23] Boping Wu; Haogang Wang, "Methods and designs for improving the signal integrity for 3D electrical interconnects in high performance IC packaging," 2011 IEEE Electrical Design of Advanced Packaging and Systems Symposium (EDAPS), pp.1–4, Dec. 2011.

[24] B. Wu and L. Tsang, "Signal integrity analysis of package and printed circuit board with multiple vias in substrate of layered dielectrics," IEEE Transaction on Advanced Packaging, vol. 33, no. 2, pp. 510-516, May 2010.

[25] Srinivasan, K.; Muthana, P.; Mandrekar, R.; Engin, E.; Choi, J.; Swaminathan, M., "Enhancement of signal integrity and power integrity with embedded capacitors in high-speed packages", ISQED '06. 7th International Symposium on Quality Electronic Design, March 2006.

[26] Eudes, T.; Ravelo, B.; Louis, A., "Experimental Validations of a Simple PCB Interconnect Model for High-Rate Signal Integrity," IEEE Transactions on Electromagnetic Compatibility, vol.54, no.2, pp.397–404, April 2012.

[27] Jun, F.; Xiaoning, Y.; Kim, J.; Archambeault, B.; Orlandi, A., "Signal integrity design for high-speed digital circuits: Progress and directions," IEEE Transactions on Electromagnetic Compatibility, vol. 52, no. 2, pp. 392–400, May 2010.

[28] Buckwalter, J., "Predicting microwave digital signal integrity," IEEE Transaction on Advanced Packaging, vol. 32, no. 2, pp. 280–289, May 2009.

[29] Kim, J.; Li, E.,"Special issue on PCB level signal integrity, power integrity, and EMC," IEEE Transactions on Electromagnetic Compatibility, vol. 52, no. 2, pp. 246–247, May 2010.

[30] Shang, E.; Chyan, L.; Sebastian, P., "Signal integrity analysis for high speed digital circuit," 2010 International Conference on Intelligent and Advanced Systems (ICIAS), pp.1–6, June 2010.

[31] Smith, L., "Simultaneous Switch Noise and Power Plane Bounce for CMOS Technology," Proceedings of IEEE 8th Topical Meeting on Electrical Performance of Electronic Packaging, San Diego, CA, pp. 163–165, October 1999.

[32] Chen, C.; Zhao, J.; Chen, Q., "A simulation study of simultaneous switching noise," Proceedings of Electronic Components and Technology Conference, pp. 1102–1106, 2001.

[33] Telikepalli, S.; Swaminathan, M.; Keezer, D., "Minimizing simultaneous switching noise at reduced power with power transmission lines for high-speed signaling," IEEE 21st Conference on Electrical Performance of Electronic Packaging and Systems (EPEPS), pp. 29–32, Oct. 2012.

[34] Huh, S.; Chung, D.; Swaminathan, M., "Achieving near zero SSN power delivery networks by eliminating power planes and using constant current power transmission lines," in Proceedings of Electrical Performance of Electronic Packaging and Systems, pp. 17–20, Oct. 2009.

[35] Swaminathan, M.; Engin, A., Power Integrity Modeling and Design for Semiconductor and Systems. Englewood Cliffs, NJ: Prentice-Hall, 2007.

[36] Kumar, S.; Chandramohan, G.; Van Driel, W.; Zhang, G., "Effects of crosstalk and simultaneous switching noise on high performance digital system packages," 11th International Conference on Electronic Packaging Technology and High Density Packaging (ICEPT-HDP 2011), pp. 489–494, Aug. 2010.

[37] Huh, S.; Chung, D.; Swaminathan, M., "Near zero SSN power delivery networks using Constant Voltage Power Transmission Lines," IEEE Electrical Design of Advanced Packaging and Systems Symposium, (EDAPS 2009), pp.1–4, Dec. 2009.

[38] Telikepalli, S.; Swaminathan, M.; Keezer, D., "Minimizing Simultaneous Switching Noise at Reduced Power with Constant Voltage Power Transmission Lines for High-Speed Signaling," Submitted to The International Symposium on Quality Electronic Design (ISQED), 2013

[39] Engin, E.; Swaminathan, M.; "Power Transmission Lines: A New Interconnect Design to Eliminate Simultaneous Switching Noise," in Proceedings of The Electronic Components and Technology Conference, pp. 1139–1143, May 2008.

[40] M. Swaminathan et al., "Designing and Modeling for Power Integrity," IEEE Transactions on Electromagnetic Compatibility, Vol. 52, No. 2, pp. 288–310, May 2010.

[41] Li-Xin, W; Yu-xia, Z; Gang, Z, "Power Integrity Analysis for High-Speed PCB," First International Conference on Pervasive Computing Signal Processing and Applications (PCSPA 2010), pp.414–418, Sept. 2010.

[42] Telikepalli, S.; Kim, S; Park, S; Swaminathan, M.; Han, Y, "Managing signal and power integrity using power transmission lines and alternative signaling

schemes," IEEE Fourth Latin American Symposium on Circuits and Systems (LASCAS 2013), pp.1–4, Feb. 2013.

[43] Yang, L.; Kim, J; Oh, D.; Lan, H.; Schmitt, R., "Power Integrity Characterization and Correlation of 3D Package Systems Using ON-Chip Measurements," Proceedings of IEEE Electrical Performance of Electronic Packaging and Systems, pp.221–224, 2010.

[44] Lin, Y-H.; Chou, J.; Lu, Y-C.; Wu, T-L; Chen, H-S., "Chip-Package-Board Co-design: a DDR3 System Design Example from Circuit Designers' Perspective," Proceedings of IEEE Electrical Design of Advanced Packaging and Systems Symposium (EDAPS), pp.27–30, 2008.

[45] Ulrich, R; Brown, W, Advanced Electronic Packaging, 2nd ed., IEEE Press Series on Microelectronic Systems, 2006.

[46] Wane, S.; Kuo, An-Yu; Dos Santos, P., "Dynamic power and signal integrity analysis for chip-package-board co-design and co-simulation," European Microwave Integrated Circuits Conference (EuMIC2009), pp.527–530, Sept. 2009.

[47] Ikemiya, K.; Kanazawa, M.; Sudo, T.; Masuda, S.; Hirakawa, Y.; Wada, K., "Co-analysis of signal and power integrity of 3D stacked package using flexible printed circuits," International Symposium on Electromagnetic Compatibility (EMC EUROPE 2012), pp. 1–4, Sept. 2012.

[48] Chung,H-H.; Wu, S-J.; Hong, M-Z.; Hsu, D.; Huang, R.; Hsiao, Li; Wu, T-L., "Power Integrity Chip-Package-PCB Co-Simulation for I/O Interface of DDR3 High-Speed Memory," Proceedings of IEEE Electrical Design of Advanced Packaging and Systems Symposium (EDAPS), pp.31–34, 2008.

[49] Jae Young Choi; Swaminathan, M., "Practical aspects of modeling apertures for signal and power integrity co-simulation," 20th IEEE Conference on Electrical

Performance of Electronic Packaging and Systems (EPEPS 2011), pp.7–10, Oct. 2011.

[50] Zaw Zaw Oo; Enxiao, L; Chang, W.; Erping, L.; Kee, C.; Le-Wei, L., "Novel Co-Simulation Method for Analysis of Power Integrity and EMI in Electronic Packages with Large Number of Power/ground Vias," Electronics Packaging Technology Conference, pp.421–424, Dec. 2007.

[51] Bharath, K.; Engin, E.; Swaminathan, M.; Uriu, K.; Yamada, T., "Signal and Power Integrity Co-Simulation for Multi-layered System on Package Modules," IEEE International Symposium on Electromagnetic Compatibility, (EMC2007), pp.1–6, July 2007.

[52] Gunupudi, P.; Nakhia, M.; Achar, R., "Simulation of high-speed distributed interconnects using Krylov-space techniques," IEEE Transactions on Computer-Aided Design of Integrated Circuits and Systems, vol.19, no.7, pp.799–808, Jul 2000.

[53] Antonini, G., "SPICE equivalent circuits of frequency-domain responses," IEEE Transactions on Electromagnetic Compatibility, vol. 45, no. 3, pp. 502–512, Aug. 2003.

[54] Antonini, G.; CiccomanciniScogna, A.; Orlandi, A., "Time domain modeling of PCB discontinuities," in Electrical Engimeriflg and Elctromagnetics, Wessex Institute of Technology Press, UK, 2003.

[55] Pozar, D., Microwave Engineering, Addison-Wesley, Reading, Massachusetts, 1990.

[56] Pillage, L.; Rohrer, R., "Asymptotic waveform evaluation for timing analysis," IEEE Transactions on Computer-Aided Design of Integrated Circuits and Systems, vol. 9, no. 4, pp. 352–366, Apr 1990.

[57] Chiprout, E.; Nakhla, M., "Analysis of interconnect networks using complex frequency hopping (CFH)," IEEE Transactions on Computer-Aided Design of Integrated Circuits and Systems, vol.14, no.2, pp.186–200, Feb 1995.

[58] Achar, R.; Gunupudi, P.; Nakhla, M.; Chiprout, E., "Passive interconnect reduction algorithm for distributed/measured networks," IEEE Transactions on Circuits and Systems II: Analog and Digital Signal Processing, vol.47, no.4, pp.287–301, Apr. 2000.

[59] Min, S.; Swaminathan, M., "Efficient construction of two-port passive macromodels for resonant networks," Electrical Performance of Electronic Packaging, pp. 229–232, 2001.

[60] Choi, K.; Swaminathan, M., "Development of model libraries for embedded passives using network synthesis," IEEE Transactions on Circuits and Systems II: Analog and Digital Signal Processing, vol.47, no.4, pp.249–260, Apr. 2000.

[61] Beyene, W.; Schutt-Aine, J., "Efficient transient simulation of high-speed interconnects characterized by sampled data," IEEE Transactions on Components, Packaging, and Manufacturing Technology, vol. 21, Feb. 1998.

[62] Beyene, W., "Improving time-domain measurements with a network analyzer using a robust rational interpolation technique," IEEE Transactions on Microwave Theory and Techniques, vol.49, no.3, pp.500–508, Mar. 2001.

[63] Chakravorty, S.; Min, S.; Swaminathan, M., "Comparison between Chebyshev and power series expansion functions for interpolating data," Electrical Performance of Electronic Packaging, pp.153–156, 2001.

[64] Gustavsen, B.; Semlyen, A., "Rational approximation of frequency domain responses by vector fitting," IEEE Transactions on Power Delivery, vol.14, no.3, pp.1052–1061, Jul 1999.

[65] Min, S.; Swaminathan, M., "Construction of broadband passive macromodels from frequency data for simulation of distributed interconnect networks," IEEE Transactions on Electromagnetic Compatibility, vol.46, no.4, pp.544–558, Nov. 2004.

[66] Nussenzveig, Causality and dispersion relations, Academic Press, 1972.

[67] Triverio, P.; Grivet-Talocia, S., "On checking causality of bandlimited sampled frequency responses," in Research in Microelectronics and Electronics 2006, Ph. D., 2006, pp. 501–504.

[68] Xu, B.; Zeng, X,; He, J.; Han, D., "Checking causality of interconnects through minimum-phase and all-pass decomposition," HDP'06 Conference on High Density Microsystem Design and Packaging and Component Failure Analysis, pp. 67–69, June 2006.

[69] Morgan, C., "Solutions for Causal Modeling and a Technique for Measuring Causal and Broadband Dielectric Properties," DesignCon 2008 Conference Proceedings, IEC Publications, Feb 2008.

[70] Triverio, P.; Grivet-Talocia, S., "A robust causality verification tool for tabulated frequency data," IEEE Workshop on Signal Propagation on Interconnects, pp. 65–68, May 2006.

[71] Antonini, G.; Orlandi, A.; Ricchiuti, V., "Causality check for SI data validation," Proceedings of the 9th IEEE Workshop on Signal Propagation on Interconnects, pp. 155-158, May 2005.

[72] Tesche, F., "On the use of the Hilbert transform for processing measured CW data," IEEE Transactions on Electromagnetic Compatibility, vol.34, no.3, pp. 259–266, Aug. 1992.

[73] Rao, M.; Sarkar, T.; Anjali, T.; Adve, R., "Simultaneous extrapolation in time and frequency domains using hermite expansions," IEEE Transactions on Antennas and Propagation, vol. 47, no. 6, pp. 1108-1115, June 1999.

[74] Boche, H.; Protzmann, M., "A new algorithm for the reconstruction of bandlimited functions and their Hilbert transform," IEEE Transactions on Instrumentation and Measurement, vol. 46, no. 2, pp. 442-444, Apr 1997.

[75] Oppenheim, A.; Schafer, R.; Buck, J., Discrete-Time Signal Processing, 2nd Edition, Prentice Hall, NY, USA, 1999.

[76] Aboutaleb, H.; Barannyk, L.; Elshabini, A.; Barlow, F., "A new method for causality enforcement of DRAM package models using discrete Hilbert transforms," in 2013 IEEE Workshop on Microelectronics and Electron Devices (WMED), pp.21-24, April 2013.

[77] Boyd, J., "A comparison of numerical algorithms for Fourier extension of the first, second, and third kinds," Journal of Computational Physics, Volume 178, Issue 1, pp. 118–160, May 2002.

[78] Bruno, O., "Fast, high-order, high-frequency integral methods for computational acoustics and electromagnetics," In Topics In Computational Wave Propagation: Direct and Inverse Problems (2003), vol. 31 of Lecture Notes In Computational Science and Engineering, pp. 43–82, 2003.

[79] Bruno, O.; Han, Y.; Pohlman, M., "Accurate, high-order representation of complex three-dimensional surfaces via Fourier continuation analysis," Journal of Computational Physics, Vol. 227, Issue 2, pp. 1094-1125, Dec 2007.

[80] Boyd, J.; Ong, J., "Exponentially-Convergent Strategies for Defeating the Runge Phenomenon for the Approximation of Non-Periodic Functions, Part I: Single-

Interval Schemes," Communications in Computational Physics, Vol. 5, Issue 2-4, pp. 484–497, 2009.

[81] Huybrechs, D., "On the Fourier Extension Of Nonperiodic Functions," SIAM Journal on Numerical Analysis, Vol. 47, Issue 6, 2010, pp. 4326–4355.

[82] Lyon, M., "A Fast Algorithm For Fourier Continuation," SIAM Journal on Scientific Computing, Vol. 33, Issue 6, pp. 3241–3260, 2011.

[83] Lyon, M., "Approximation error in regularized SVD-based Fourier continuations," Applied Numerical Mathematics, Vol. 62, Issue 12, pp. 1790–1803, 2012.

[84] Lyon, M.; Bruno, O., "High-order unconditionally stable FC-AD solvers for general smooth domains II, Elliptic, parabolic and hyperbolic PDEs: theoretical considerations," Journal of Computational Physics, Vol. 229, Issue 9, pp. 3358–3381, 2010.

[85] Albin, N.; Bruno, O.; Cheung, T.; Cleveland, R., "Fourier continuation methods for high-fidelity simulation of nonlinear acoustic beams," Journal of the Acoustical Society of America, Vol. 132, Issue 4, pp. 2371–2387, 2012.

[86] Shahbazi, K.; Albin, N.; Bruno, O.; Hesthaven, J., "Multi-domain Fourier-continuation/WENO hybrid solver for conservation laws," Journal of Computational Physics, Vol. 230, Issue 24, pp. 8779–8796, 2011.

[87] Albin, N.; Bruno, O., "A spectral FC solver for the compressible Navier-Stokes equations in general domains I: Explicit time-stepping," Journal of Computational Physics, Vol. 230, Issue 16, pp. 6248-6270, 2011.

[88] Lyon, M.; Picard, J., "The Fourier approximation of smooth but non-periodic functions from unevenly spaced data," Advanced Computational Math, ((submitted)).

[89] Lyon, M., "Sobolev smoothing of SVD-based Fourier continuations," Applied Mathematics Letters, Vol. 25, Issue 12, pp. 2227-2231, 2012.

[90] Dienstfrey, A.; Greengard, L., "Analytic continuation, singular-value expansions, and Kramers-Krönig analysis," Inverse Problems, Vol. 17, Issue 5, pp. 1307–1320, 2001.

[91] Knockaert, L.; Dhaene, T., "Causality Determination and Time Delay Extraction by Means of the Eigenfunctions of the Hilbert Transform," in 12th IEEE Workshop on Signal Propagation on Interconnects, pp. 1–4, May 2008.

[92] Triverio, P.; Grivet-Talocia, S.; Nakhla, M.S.; Canavero, F.G.; Achar, R., "Stability, Causality, and Passivity in Electrical Interconnect Models", IEEE Transactions on Advanced Packaging, vol. 30, no. 4, pp. 795–808, Nov. 2007.

[93] Kim, D.; Eo, Y., "S-parameter-measurement-based-time-domain signal transient and crosstalk noise characterizations of coupled transmission lines," IEEE Transactions on Advanced Packaging, vol. 32, no. I, pp. 152–163, Feb 2009.

[94] Mandrekar, R.; Swaminathan, M., "Causality enforcement in transient Simulation of passive networks through delay extraction," in Proceedings of Signal Propagation on Interconnects, pp. 25–28, 2005.

[95] Dym, H.; McKean, H., Fourier Series and Integrals, Series of Probability and Mathematical Statistics Monograph. Academic Press, 1985.

[96] Krönig, R., "On the theory of dispersion of x-rays," Journal of Optical Society of America, vol. 12, no. 6, pp. 547–557, 1926.

[97] Kramers, H., "La diffusion de la lumiere par les atomes," Atti Cong. Intern. Fisica (Transactions of Volta Centenary Congress) Como, vol. 2, pp. 545–557, 1927.

[98] Beltrami, E.; Wohlers, M., Distributions and the Boundary Values of Analytic Functions. Academic Press, 1966.

[99] Triverio, P.; Grivet-Talocia, S., "Robust Causality Characterization via Generalized Dispersion Relations," IEEE Transactions on Advanced Packaging, vol.31, no.3, pp.579–593, Aug. 2008

[100] Wojnowski, M.; Sommer, G.; Weigel, R., "Device Characterization Techniques Based on Causal Relationships," IEEE Transactions on Microwave Theory and Techniques, vol. 60, no. 7, pp. 2203–2219, July 2012.

[101] Tesche, F., "On the use of the Hilbert transform for processing measured CW data," IEEE Transactions on Electromagnetic Compatibility, vol. 34, no. 3, pp. 259–266, Aug 1992.

[102] Bradie, B., A Friendly Introduction to Numerical Analysis. Pearson Prentice Hall, 2005.